

POLITECNICO DI TORINO

Master's Degree in Nanotechnologies for ICTs
Bachelor's Degree in Electronic Engineering



Master's and Bachelor's Double Degree Thesis

Fabrication of an integrated optical resonator for microwave to optical conversion on an atom chip

Supervisors

Prof. Matteo COCUZZA

Prof. Angelo ANGELINI

Candidate

Mateo ROSERO REALPE

Sep 2023

Abstract

Currently quantum computing has proven to make fast and accurate logical calculations and promises to drastically change the field of computing. One of the main limitations are the short coherence times of qubits, which precludes information storage, and the possibility of making distant communications between quantum registers that is challenging using microwave photons (these are resonant with qubit transitions). The MOCA project proposes the use of an integrated chip combining superconducting resonators with optical waveguides and cavities that converts the microwave photons to optical photons. The chip is then coupled to an ensemble of cold atoms for the long term storage of the information. In this way, the fabrication of a Radio Frequency (RF) resonator and a photonic resonator play an important role in the creation of the device. The project is part of the QuantERA programme, created to develop quantum technologies in Europe. However, the tasks to accomplish the goal are divided into 5 research groups in which experimental and theoretical physics are applied. INRIM is in charge of fabricating the RF and photonic resonators, and in my thesis I focused on developing the photonic components. The resonator consists of 3 parts: a waveguide in which the optical photons are confined, a cavity with bragg reflectors to create a resonator for efficient photon conversion and a grating to couple the signal from the waveguide to the optical fibers. The operating wavelength chosen is 760 nm. For the good confinement of the wave in the waveguide, a high refractive index material with low losses is needed. We chose Silicon Nitride (SiN), and we modified the recipe for deposition in order to increase the refractive index up to 2.4. The SiN thin films are deposited by Chemical Vapor Deposition (CVD) on a dielectric substrate (in this case, thick corning glass). We calibrated the deposition process and measured the deposition rate in order to obtain a final thickness of 200 nm, which is the thickness required for the waveguides. We optimized the final geometry for the waveguides and the gratings by means of a Finite Element Method commercial software and the obtained structures were replicated in a CAD software for Electron Beam Lithography (EBL). The lithographic process was followed by an Aluminum deposition to obtain an hard mask that could be used in a Reactive Ion Etching step to remove the exceeding Silicon Nitride. For the Reactive Ion Etching (RIE) step we optimized a recipe that approximates to a Silicon Etching recipe more than a SiN recipe, and taking into account the need of a conformal structure, a pseudo-bosch etching was used. Secondly is the grating coupler, whose parameters can be calculated considering the angle of incidence of the light into the grating and the Bragg's condition for the proper diffraction of the light. Finite Element Method (FEM) modeling was performed to optimize the structure. Thirdly, we want to

confine light in a microcavity by fabricating Distributed Bragg Reflectors (DBR) along the waveguide. In such a way, we want to increase the photon density within the cavity and enable the conversion of microwave photons radiated by the cold atom ensemble into optical ones. As an alternative route for the light confinement and manipulation, we also considered using a metasurface made of SiN nanopillars. FEM models show that such structures can sustain resonant modes with a quality factor as high as 10^5 .

Acknowledgements

I would like to express my deepest gratitude to my supervisors, Matteo Cocuzza and Angelo Angelini, for their guidance, support, and invaluable feedback throughout the development of my thesis. Their expertise and encouragement have been instrumental in shaping this thesis. I would like to express my gratitude to the professors and assistants from Politecnico di Torino, where I pursued my master's degree, and Universidad Javeriana de Bogotá, where I did my bachelor's degree. Thanks to the double degree program offered by my university in my country, I was able to travel and achieve this accomplishment.

In addition, I would like to express my heartfelt gratitude to my family and friends for their unwavering support, encouragement, and love throughout this journey. Their constant motivation and understanding have been instrumental in helping me overcome the challenges and obstacles that I faced during the research process. I am grateful for their patience, kindness, and unwavering belief in me. This thesis would not have been possible without their support, and I am forever indebted to them.

Mateo Rosero Realpe, Torino, October, 2023

Table of Contents

List of Tables	VII
List of Figures	VIII
Acronyms	XIII
1 Introduction	1
1.1 MOCA project	1
1.2 Working principle	2
1.3 MW and optical waveguides at INRIM	3
1.4 Project Workflow	3
2 Device design	5
2.1 Macro design	5
2.2 Waveguide	5
2.2.1 Definition and working principle	5
2.2.2 Waveguide Modes	6
2.2.3 Theoretical calculations	8
2.2.4 Analytic calculation in 1D and 2D	8
2.2.5 Simulation with COMSOL	9
2.2.6 Chosen design parameters	10
2.3 Grating coupler	11
2.3.1 Definition and working principle	11
2.3.2 Theoretical calculations	13
2.4 Resonant cavity	16
2.4.1 Definition and working principle	16
2.4.2 Theoretical calculations	17
2.4.3 Analytic calculation	19
3 Material Deposition and Characterization	22
3.1 Chemical Vapor Deposition	22

3.1.1	Description of CVD	22
3.1.2	Parameters to increase the refractive index	24
3.2	Ellipsometry	25
3.2.1	Description	25
3.2.2	Results	26
3.3	Optical Profilometry	26
3.3.1	Description	26
3.3.2	Results	29
3.4	Stylus Profilometry	29
3.4.1	Description	29
3.4.2	Results	30
3.5	Deposition rate comparison	30
3.6	X-ray Photoelectron Spectroscopy	32
3.6.1	Description	32
3.6.2	Material Composition	33
4	Lithography	35
4.1	Optical Lithography	35
4.1.1	Description	35
4.1.2	Test designs	37
4.2	Sputter Deposition	38
4.2.1	Description	38
4.2.2	Used recipe	39
4.2.3	Lift off	40
4.3	Scanning Electron Microscopy	41
4.3.1	Description	41
4.4	Electron Beam Lithography	43
4.4.1	Description	43
4.4.2	NPGS software	44
4.4.3	CAD design	44
4.4.4	First test lithography	45
4.4.5	Second test lithography	46
4.4.6	Combination with Photolithography	47
4.4.7	Isolated Resonator lithography	48
5	Etching	51
5.1	Reactive Ion Etching	51
5.1.1	Description	51
5.1.2	Endpoint detector	52
5.1.3	Etching of SiN	53
5.1.4	Etching rate	56

5.1.5	Final structures and problems	57
6	Device characterization	61
6.1	Waveguide and grating response	62
7	Alternative strategies to confine light	65
7.1	Working principle of the metasurface	66
7.2	Electric and magnetic poles in the metasurface	68
7.3	Metasurface implementation	68
A	Code implementation for CAD design	71
	Bibliography	85

List of Tables

3.1 Gas flow rates for Silicon Nitride deposition	24
---	----

List of Figures

1.1	Conceptual device. Microwave resonator in gray, optical resonator in blue and cloud of alkali atoms in red.	1
1.2	Schematics of the system: an ensemble of atoms trapped on a superconducting chip near a coplanar waveguide cavity converts the microwave photon of the cavity to an optical photon fed into a fiber waveguide. [2]	2
1.3	Flow chart process for the optical resonator design	4
2.1	General macro design	6
2.2	Planar waveguides guide light only in the vertical directions, allowing 2 degrees of freedom. Channel waveguides guide in two dimensions, thus allowing only 1 degree of freedom	6
2.3	Parts of a waveguide	7
2.4	Calculation of different modes of the waveguide with MATLAB	9
2.5	Product of the fields calculated with the MATLAB code.	10
2.6	COMSOL simulation of the waveguide	11
2.7	Grating coupler cross section. Waveguide is to the left of the axis, while the grating coupler is to the right	12
2.8	Bragg condition for the grating coupler [7].	14
2.9	Side view of grating coupler in 3D to display the coupling angle.	15
2.10	Grating coupler seen from above.	16
2.11	DBR resonator (simplified).	17
2.12	DBR resonator diagram with both reflectivities.	18
2.13	Reflectivity of the DBR mirror with respect to the differential wavelength [15]	19
2.14	Material numbers for the optical resonator	20
2.15	Results for TMM simulation with MATLAB for different number of grating periods going from 2 to 10. This simulation is done without considering the propagation losses ($\alpha = 0$)	21
3.1	Dissociation process for the generation of strongly reactive free radicals	23

3.2	A sample of corning glass with a layer of Silicon Nitride above . . .	25
3.3	Diagram of the working principle of Ellipsometry [20]	25
3.4	Plot of amplitude ratio Ψ , and the phase difference Δ with respect to the wavelength in nm of one of the SiN samples. The Cauchy model has been used for the model fitting	27
3.5	Plot of real refractive index (n) and the extinction coefficient (k) with respect to the photon wavelength in nm	27
3.6	Plot of thickness vs deposition time with data from the ellipsometer	28
3.7	Working principle of optical profilometer. [23]	28
3.8	Measurement of the step height at the corner of one sample with optical profilometer	30
3.9	Plot of thickness vs deposition time with data from the optical profilometer	31
3.10	Plot of thickness vs position on x	31
3.11	Plot of thickness vs position on x	32
3.12	XPS results	34
4.1	General photolithographic process	36
4.2	Photolithography test after developing. Measured with Optical profilometer. It can be seen that the height of the resist is around $1.5\mu m$	38
4.3	Sputtering deposition chamber with all the component	39
4.4	General lift-off process	41
4.5	General lift-off process with image reversal	42
4.6	Python program for the design of the optical resonator (the values on the picture are example values). Code on appendix A	45
4.7	CAD design of a short waveguide test.	46
4.8	SEM images showing the result of the lithographic process of the grating coupler and waveguide together	46
4.9	CAD design of a long waveguide. The coupling grating seem to be completely fill but is due to the sampling of the image as the grating lines are thin	47
4.10	Result of the lithographic process with separated CAD designs. A displacement and a rotation can be seen between the grating coupler and the waveguide.	48

4.11	Result of the lithographic process with the alignment process combining optical lithography and EBL. At left, the waveguide and alignment marks mask can be seen with high contrast as these are made of aluminum, while at the center the grating coupler is made of resist. At right, it can be seen that the alignment was successful and good coupling of the grating with the waveguide could be achieved thanks to this process.	49
4.12	CAD of the resonator with two additional short waveguides	49
4.13	Result of EBL lithography of the resonator	50
5.1	RIE test for the circles and squares lithography. Data taken with optical profilometer	54
5.2	RIE test for EBL lithography using resist ma-n2401 as a mask	55
5.3	RIE test for EBL lithography using resist Aluminum as a mask	55
5.4	RIE test for EBL lithography using resist ma-n2405 as a mask	56
5.5	RIE test for EBL lithography using resist ma-n2405 as a mask. At the left image the structure still have the resist mask above. At the right the resist mask is removed	57
5.6	Reflectance intensity data when etching a sample with a layer of SiN	58
5.7	RIE test for EBL lithography of optical resonator	58
5.8	RIE of grating coupler aligned with waveguide	59
5.9	RIE of grating coupler aligned with waveguide	60
6.1	3D model side view of the device and the 2 optic fibers for the input and output signal	62
6.2	Simplified setup for the waveguide test	63
6.3	Waveguide test for perpendicular coupling. At the left image the spot of the input laser beam is big enough to illuminate a great part of the grating. At the right image, the spot is reduced and the image exposure time is increased in order to see the entire waveguide, but no emitted light is seen at the output	63
6.4	Sample being illuminated with the laser spot above the grating. The waveguide is horizontal, thus there are two laser spots at left and right side of the sample	64
6.5	Illuminated sample with condensor. At the left image, the sample is being illuminated with a focusing beam outside the grating coupler. At the right image, the laser spot is inside the grating, the sample glows due to the light confinement inside the substrate since the glass substrate is acting as a waveguide.	64

7.1	At the left, the unit cell consisting of a diamond nanopillar on a glass substrate with the indicated dimensions: D is the diameter of the cylinder, h is the height of the cylinder and P is the pitch. At the right the Transmittance response is shown at different cylinder heights	66
7.2	Idea for a resonator composed by a metasurface (at the bottom) and a optical fiber (at the top), where the fiber acts as a mirror at the interface	66
7.3	Rayleigh scattering description	67
7.4	Mie scattering generated poles: Electric dipole, Magnetic dipole, Electric quadrupole, Magnetic quadrupole, etc	67
7.5	Lateral view of the cylinder electric (E) and magnetic (H) fields. The flux lines show the creation of two magnetic dipoles and one magnetic quadrupole	69
7.6	SEM image of the sample after doing RIE process on it. An EBL patterning of a circle matrix was done before to use the resist as a mask for etching	69
7.7	Comparison of simulated and experimental results. At the left image, the simulated optical transmittance with COMSOL. At the right image, the experimental optical transmittance of the metasurface. There are 3 resonance frequencies where the reflection is increased	70

Acronyms

PR

Photoresist

CVD

Chemical Vapor Deposition

PECVD

Plasma Enhanced Chemical Vapor Deposition

ICP

Inductively Coupled Plasma

RF

Radio Frequency

EBL

Electron Beam Litography

PVD

Physical Vapor Deposition

RIE

Reactive Ion Etching

INRIM

Istituto Nazionale di Ricerca Metrologica

DBR

Distributed Bragg Reflector

MFD

Mode Field Diameter

FSR

Free Spectral Range

XPS

X-ray Photoelectron Spectroscopy

NPGS

Nanometer Pattern Generation System

SEM

Scanning Electron Microscopy

TMM

Transfer Matrix Method

PDE

Partial Differential Equation

Chapter 1

Introduction

1.1 MOCA project

The MOCA project (Integrated Microwave-to-Optical Conversion by Atoms on a superconducting chip) is a project made to solve the problem of short coherence times on superconducting qubits which preclude long-term storage of quantum information and hinders the transport of microwave photons which prevents long distance coupling of quantum registers. Cold gases of alkali atoms have a smaller processing speed than superconducting qubits, thus they can well perform these two tasks. [1]

In this project alkali atoms are incorporated into a superconducting hybrid device. The project aims at the coherent conversion of microwave to optical signals on an integrated chip compatible with superconducting quantum processors and optical communication networks. These hardware components will form the basis for long-distance quantum communication between superconducting quantum (sub)processors mediated by optical photons.

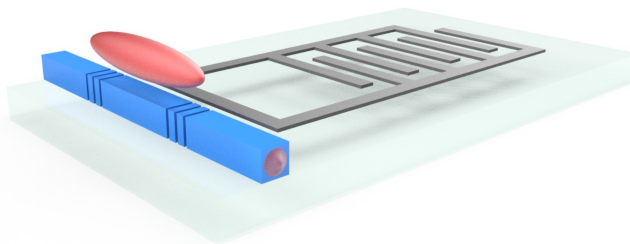


Figure 1.1: Conceptual device. Microwave resonator in gray, optical resonator in blue and cloud of alkali atoms in red.

1.2 Working principle

Cold atomic systems, have unique advantages over other approaches for microwave to optical conversion. Atomic spin ensembles can couple to superconducting microwave resonators to realize quantum memory in the long-lived hyperfine manifold of levels. The microwave photon is confined in a coplanar waveguide resonator, while a cold atomic ensemble is trapped near the antinode of the microwave cavity mode at a distance of several tens of microns from the surface of the atom chip (fig 1.2). Rydberg transitions are employed between the atomic states that strongly couple to the microwave cavity field. [2]

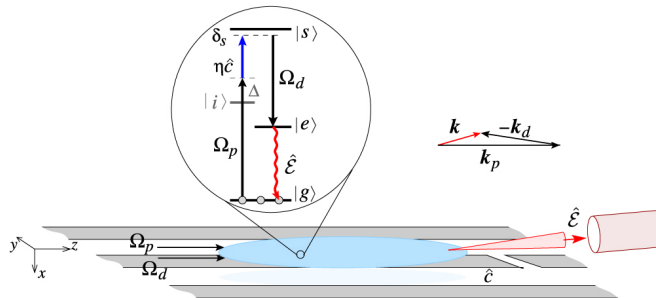


Figure 1.2: Schematics of the system: an ensemble of atoms trapped on a superconducting chip near a coplanar waveguide cavity converts the microwave photon of the cavity to an optical photon fed into a fiber waveguide. [2]

A stimulated Raman process triggered by a coupling laser pulse converts the collective spin excitation of the atoms to an optical photon emitted predominantly in the phase-matched direction, that is then collected into a single-transverse-mode optical waveguide. The waveguide can then transmit the photon encoding the quantum information to a distant atomic ensemble, where a reverse process, equivalent to dynamical light storage in an electromagnetically induced transparency medium, will coherently convert the optical excitation to a collective microwave spin excitation. [3]

A well-known approach for efficient photon collection is to place the atoms or other emitters into a resonant cavity with sufficiently strong coupling so that the Purcell enhancement [4] of the photoemission rate into the cavity mode largely exceeds the free-space spontaneous decay rate with the photon emitted in a random direction.

1.3 MW and optical waveguides at INRIM

INRIM will develop in a few iterations a room temperature atom chip. The design for this chip will include both a gold coplanar microwave transmission line and a Si_3N_4 nanowaveguide cavity integrated in the $10\mu m$ gap of the microwave line. In addition, the design will also include a gold surface required for the atom transport. The couplers design will be optimized to achieve injection coupling efficiency above 70%.

In parallel, INRIM will fabricate a superconducting microwave coplanar waveguide cavity (parameters: 6.8GHz, Q 104-105 at T=4K) and wire components for magnetic trapping of Rubidium atoms. The superconducting chip and microwave cavity will be fabricated with Niobium thin film technology on polished sapphire chip surfaces.

Finally, INRIM will integrate on the superconducting chip an optical waveguide cavity in the gap of the coplanar microwave cavity.

In this thesis, we will focus on the development of the optical waveguide and optical resonator.

1.4 Project Workflow

The device fabrication requires a combination of different micro and nanofabrication techniques, and each process needs to be optimized for obtaining the required structure. The general flow chart of the fabrication process is present in figure 1.3. A feedback from one process to another is required as each step can influence the following steps, and therefore the full process has to be adjusted consequently.

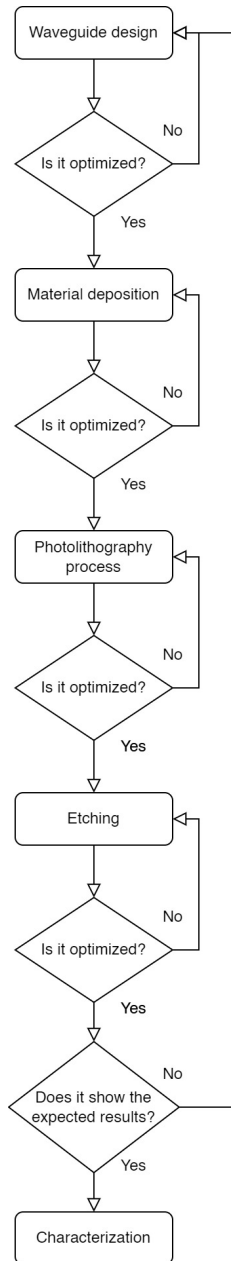


Figure 1.3: Flow chart process for the optical resonator design

Chapter 2

Device design

2.1 Macro design

First of all, the components for the optical waveguide in the project are (they will be explained in depth after):

1. Waveguide
2. Grating coupler
3. Resonant Cavity

All the components will be located in one layer only, which will be made of Si_3N_4 as it has a high refractive index. Since we want a waveguide capable of confine the light, this must have a higher refractive index than the surroundings, thus the chosen substrate is made of glass ($n \approx 1.5$). Additionally to this, the nominal wavelength of the optical photons will be $\lambda = 760nm$.

The general design is presented in the figure 2.1. It is important to known that the dimensions are exaggerated for better understanding since real dimension could be larger. For this design we need a cavity in the middle of the waveguide, a waveguide and 2 grating couplers to couple the signal to the exterior, but the in-depth explanation of each part is done in the following sections.

2.2 Waveguide

2.2.1 Definition and working principle

An optical waveguide is a structure that directs light by limiting the area in which it can travel. It is typically made up of a region with a higher refractive index than its surroundings, known as the cladding. However, light can also be guided

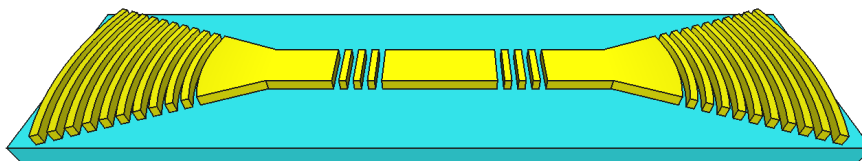


Figure 2.1: General macro design

through other means, such as reflection at metallic interfaces or by using photonic crystal structures. Certain waveguides also utilize plasmonic effects in metals. [5]

Most waveguides (included the one in MOCA's project) exhibit two-dimensional guidance, thus restricting the extension of guided light in two dimensions and restricting the propagation essentially to one dimension only 2.2.

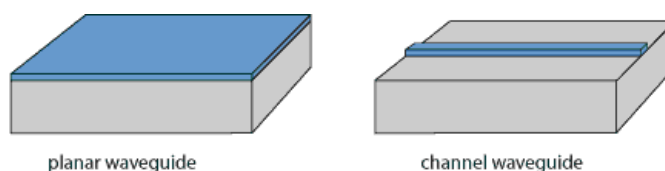


Figure 2.2: Planar waveguides guide light only in the vertical directions, allowing 2 degrees of freedom. Channel waveguides guide in two dimensions, thus allowing only 1 degree of freedom

Channel waveguides can be fabricated on semiconductor, crystal, and glass materials using lithographic techniques combined with epitaxy, ion exchange, or thermal diffusion. Another approach is to create a buried waveguide by growing an extra layer on top of the waveguide. Typically, waveguides consist of three main components: the cladding, the core (where the wave is transmitted), and the substrate.

2.2.2 Waveguide Modes

In the context of optics, it is typical to analyze the field distribution of light at a specific optical frequency and polarization in a plane that is perpendicular to the direction of propagation. The field distributions that remain unchanged during propagation, except for a common phase shift, are referred to as waveguide modes. Each mode is characterized by a propagation constant, which has an imaginary part that represents the phase delay per unit distance of propagation. In addition to guided modes, optical fibers also support a significant number of unguided modes, known as cladding modes, which are not confined to the vicinity of the fiber core.



Figure 2.3: Parts of a waveguide

Any initial field distribution of light injected into a waveguide can be expressed as a linear combination of the field distributions of the guided waveguide modes. The remaining part of the field distribution, which cannot be represented as such a combination, corresponds to light that cannot be guided. However, depending on the type of waveguide, this unguided light may propagate in the cladding or may be reflected.

a single-mode waveguide is one that can only guide a single transverse mode and no higher-order modes. This type of waveguide is characterized by a small transverse spatial extension or a small refractive index difference (i.e., small numerical aperture). The numerical aperture can be calculated as:

$$NA = \sqrt{n_{core}^2 - n_{cladding}^2}$$

This means that if the refractive index of the core is the same as the cladding, there will be no confinement of the light.

The field distribution after a specific propagation distance consistently resembles the constant mode field distribution, regardless of the initial field distribution. This indicates that the unguided modes have been eliminated. However, multimode waveguides are capable of accommodating multiple guided modes, sometimes even numerous ones.

In certain waveguides, there are modes that possess highly asymmetric intensity profiles. It is possible for guided modes to exist exclusively for one polarization direction, or for the modes to exhibit significantly different properties for different polarization directions. In our specific scenario, we will be constructing an asymmetric waveguide with a cladding refractive index that differs from that of the substrate.

The requirements for our waveguide are:

1. The waveguide should be single-mode in the z axis.
2. The waveguide should fulfill the other requirements given by different factors for the MOCA project. For example, one of them is that the waveguide shouldn't be so thin since part of the field must be outside the waveguide with the aim of interacting with the cold atoms.

2.2.3 Theoretical calculations

To design the thickness of the waveguide, what we can do is using the next theoretical formulas to calculate the number of modes of the waveguide [6]:

$$M_{TE} = \left(\frac{V}{\pi} - \frac{1}{\pi} \arctan \sqrt{a_{TE}} \right)_{int}$$

$$M_{TM} = \left(\frac{V}{\pi} - \frac{1}{\pi} \arctan \sqrt{a_{TM}} \right)_{int}$$

Where M_{TE} is the number of transverse electric modes and M_{TM} is the number of transverse magnetic modes. int means to round the result number to the nearest integer larger than the value. V is the normalized frequency given by:

$$V = \frac{2\pi}{\lambda} D \sqrt{n_{core}^2 - n_{sub}^2}$$

Where D is the thickness of the core. And the transversal electric and magnetic symmetry factor:

$$a_{TE} = \frac{n_{sub}^2 - n_{clad}^2}{n_{core}^2 - n_{sub}^2} \geq 0$$

$$a_{TM} = a_{TE} \frac{n_{core}^4}{n_{clad}^4} \geq 0, a_{TM} > a_{TE}$$

n_{sub} , n_{core} and n_{clad} are the substrate, core and cladding refractive indexes respectively.

Considering all of this, we can do the calculation of the required thickness to obtain a single mode waveguide in the transverse electric mode (M_{TE}). Since at the beginning the refractive index of the real material is unknown, we assume a generic refractive index for Silicon Nitride ($n \approx 2.4$), which is the chosen material for the project. Finally, the maximum thickness for a single-mode waveguide is $t = 239nm$

2.2.4 Analytic calculation in 1D and 2D

For the procedure of the design with analytic calculation we followed the procedure given by the book *Silicon Photonics Design* [7] which is the following:

1. In order to determine the slab waveguide modes, one-dimensional calculations are performed. The analytical method solver in 1D implemented on MATLAB [7] is used to solve the Maxwell equations by zero finding. The thickness of the waveguide is chosen based on the requirement of having a single-mode waveguide for TE and TM.

2. To meet the requirements, a suitable waveguide width must be found for the given thickness. It is not mandatory for the width to have a single mode, as it can be challenging to achieve such small waveguide width dimensions with a large length using lithographic processes. The effective index method implemented on MATLAB [7] is used to determine the appropriate waveguide width.
3. Some other considerations like waveguide bend loss or substrate leakage could be considered (these are not considered in this thesis).

Taking into account the requirement for a single-mode waveguide on z axis, the maximum thickness is $t = 230\text{nm}$. The results of the simulation are present in the figure 2.4 and figure

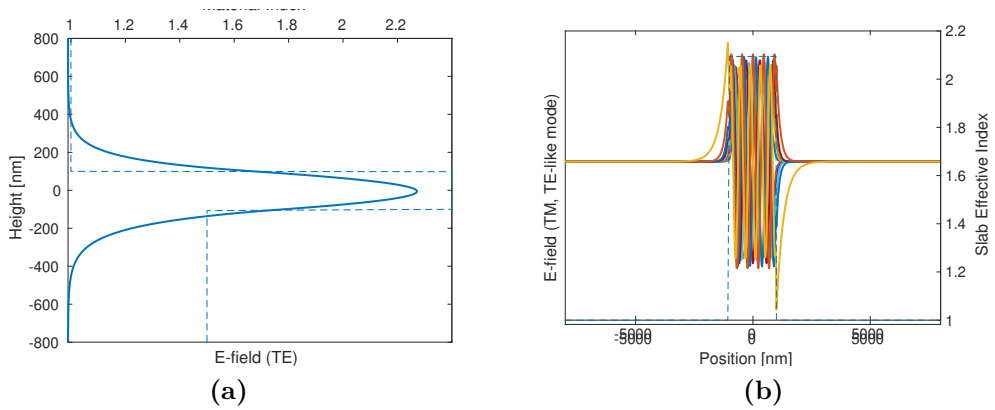


Figure 2.4: Calculation of different modes of the waveguide with MATLAB: (a) Calculation of the Electric field for the z axis (height). The dotted line represents the material index, which is not symmetrical as the substrate and cladding refractive index differ. (b) Calculation of the Electric field for the x axis (width). The dotted line represents the material index, which is symmetrical.

From the previous simulation, the effective index of the first mode is $n_{eff} = 2.10$.

2.2.5 Simulation with COMSOL

Comsol Multiphysics is a software package that is used for finite element analysis, solver, and simulation of various physics and engineering applications, particularly those involving coupled phenomena and multiphysics. This software provides conventional physics-based user interfaces and coupled systems of partial differential equations (PDEs). It also offers a unified workflow for electrical, mechanical, fluid, acoustics, and chemical applications. [8]

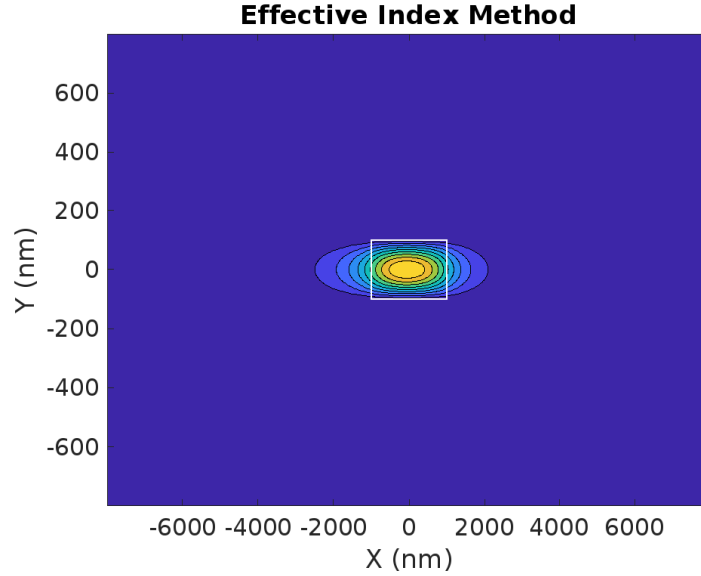


Figure 2.5: Product of the fields calculated with the MATLAB code.

The RF module is a tool that helps optimize design by analyzing the effects of electromagnetic wave propagation and resonance effects in high-frequency applications. It is used to understand and predict the performance of devices in the RF, microwave, and millimeter-wave industries. [9]

In this program with the help of the RF Module, we simulated the waveguide with the next parameters:

1. Free space wavelength: $\lambda = 760nm$
2. Waveguide width: $W = 2\mu m$
3. Waveguide thickness: $t = 200nm$
4. SiN refractive index: $n_{core} = 2.4$
5. Substrate refractive index: $n_{subs} = 1.5$

The results for the first mode can be seen in the figure 2.6. The results of the simulation gives us the effective refractive index of $n_{eff} = 2.09$, whose value can be used to do the respective calculations. It is important to see that the value is not so different from the one calculated with MATLAB in the analytical calculation.

2.2.6 Chosen design parameters

At the end, considering the requirements for the waveguide and doing the comparison for the different calculations, the final chosen thickness of the waveguide is $t =$

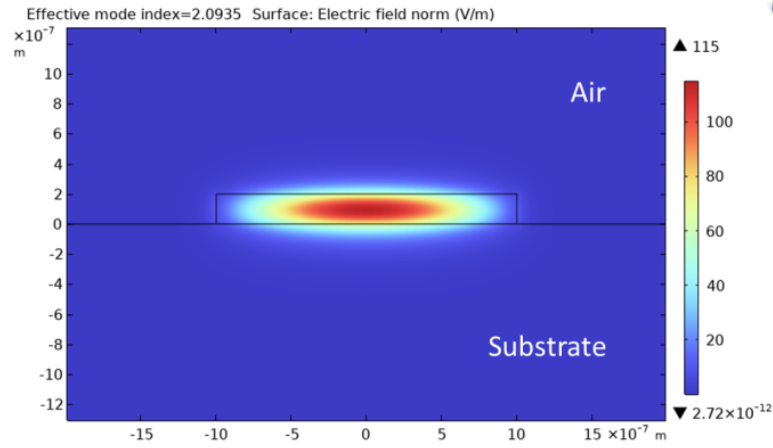


Figure 2.6: COMSOL simulation of the waveguide

200nm. While the width is not a fixed value but can be chosen between $w = 0.5\mu\text{m}$ to $w = 5\mu\text{m}$. The length on the other hand varies in the fabrication process of the waveguide to measure the losses of the waveguide at different lengths.

2.3 Grating coupler

2.3.1 Definition and working principle

A grating coupler is a structure that can diffract light from a waveguide to free-space and vice-versa. It is used as an Input/Output device to couple light between fiber (or free-space) and sub-micrometer waveguides. The structure is periodic in nature and is capable of diffracting light in-plane and out-of-plane. The figure 2.7 is a cross-section diagram of a shallow-etched grating coupler design in a silicon-on-insulator wafer [7].

The following are the parameters of the grating coupler:

1. The coupler consists of a silicon waveguide core, a top cladding (air) and a substrate (glass). The effective index of the slab waveguide is n_{eff}
2. Λ is the spatial period of the grating.
3. W is the width of the grating teeth
4. ff is the fill factor (also called duty cycle), defined as: $ff = W/\Lambda$
5. ed is the etch depth of the grating

6. θ_c is the angle between surface normal and the propagation direction of the diffracted light, in the cladding (air).

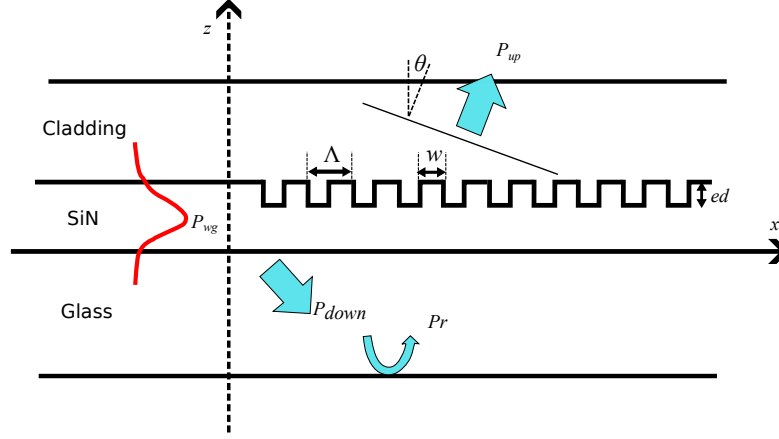


Figure 2.7: Grating coupler cross section. Waveguide is to the left of the axis, while the grating coupler is to the right

When the light is traveling through the waveguide, it will arrive to the output grating coupler, where P_{wg} is the optical power of the input light; P_{up} and P_{down} indicate the power that goes up and the power that penetrates down into the wafer. The power that is coupled into the optical fiber's fundamental mode is P_{fiber} .

The performance of the grating coupler can be described by the following parameters:

1. Directionality: the ratio between the power diffracted upwards (P_{up}) and the input power from the waveguide (P_{wg}), which is usually expressed in decibels: $10\log_{10}(P_{up}/P_{wg})$.
2. Insertion loss (coupling efficiency): is the ratio between the power coupled into the fundamental mode of the fiber (P_{fiber}) and the input power from the waveguide (P_{wg}). Expressed in dB is: $10\log_{10}(P_{fiber}/P_{wg})$.
3. Penetration loss: the ratio between the power lost in the substrate and the input power from the waveguide: $10\log_{10}(P_{down}/P_{wg})$.
4. Reflection to the waveguide: due to the refractive index contrast between the SiN wire waveguide and the grating, part of the input light from the waveguide will be reflected back into the waveguide. The ratio between the reflected power and the input power from the waveguide is called back reflection to the waveguide, also called return loss. Expressed in dB is: $10\log_{10}(P_{back-wg}/P_{wg})$. This reflection is unwanted since it will cause Fabry-Perot oscillations [10] by reflecting back and forth between the input and the output grating couplers.

5. Reflection to the fiber: for the input grating couplers, part of the input light will be reflected back to the fiber. Also referred to as optical return loss and given in dB as: $10\log_{10}(P_{back-fiber}/P_{in-fiber})$.

6. Bandwidth

2.3.2 Theoretical calculations

The grating operation can be explained by the Huygens-Fresnel principle, which describes the constructive and destructive interference that occurs when the wavefront is scattered by the diffraction of light from the grating teeth [7]. Two cases can appear with the grating coupler:

1. When the optical wavelength inside the grating matches its period, the first-order diffraction will propagate vertically and the second-order diffraction will propagate back to the waveguide. However, in practice, back-reflection is undesired since it can lead to Fabry-Perot oscillation between the input coupler and output coupler. To avoid the second-order diffraction back to the waveguide, the grating is detuned and the fiber has a small angle to the normal of the grating surface.
2. When the optical wavelength inside the grating is smaller than the grating period, the output wave will propagate at an angle. In this case, there is no second-order reflection.

The wave incident on the grating is a guided wave propagating in a slab waveguide, with a direction of propagation in the same plane as the grating, and is normal to the grating teeth. The waveguide propagation constant is:

$$\beta = n_{eff}k_0 = \frac{2\pi n_{eff}}{\lambda_0}$$

Where λ_0 is the optical wavelength, and n_{eff} is the effective index of the slab waveguide. The periodicity of the grating is described by:

$$K = \frac{2\pi}{\Lambda}$$

Where Λ is the grating period. Higher-order diffraction gratings can be considered by using $m \cdot K$. The general form of the Bragg condition can be expressed as:

$$\beta - k_x = m \cdot K$$

Where k_x is the component of the wave vector of the diffracted wave in the direction of the incident wave. The diffracted wave is travelling in the cladding with an

Choosing a fill factor of 50% for an incident angle of $\theta_c = 20^\circ$, the final period of the grating is calculated to be approximately $\Lambda = 628nm$, then the linewidth of each slab is $\Lambda \cdot ff = 314nm$ (fig 2.9). These results are only the parameters for the radial dimension, while some others are missing.

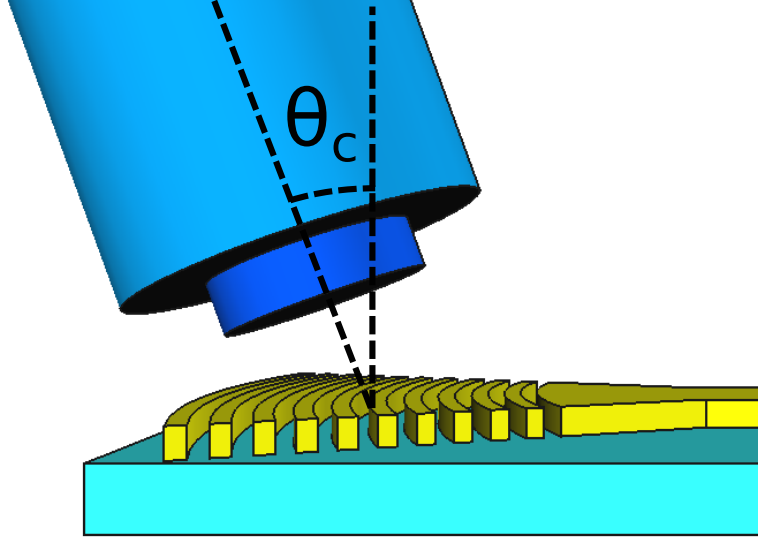


Figure 2.9: Side view of grating coupler in 3D to display the coupling angle.

Considering the paper by Lirong Cheng [11], as the grating coupler interfaces the fiber mode directly, the grating width at y-direction is usually comparable to the Mode Field Diameter (MFD) [12] of the field inside the fiber. This means that taking into account we are using a optic fiber from thorlabs [13] for wavelengths in the range $600nm < \lambda < 860nm$, the MFD is approximately $MFD \approx 5\mu m$. When transitioning light to a single-mode waveguide, a tapered waveguide is typically used. If the propagating mode only changes its size and shape in this transition, without radiating it outside the waveguide or converting to other higher-order waveguide modes, then the energy is conserved. For an adiabatic transition to occur in a linear tapered waveguide, its geometric parameters must satisfy certain conditions:

$$\theta_{taper} < \frac{\lambda}{2Wn_{eff}}$$

Where θ_{taper} is the taper angle, W is the varying waveguide width and n_{eff} is the corresponding mode effective index. However, with this method we would require a long distance for the tapered waveguide. To reduce the footprint of the grating coupler, a focused grating coupler is used, as shown in the figure 2.10. Where d_0

has a value comparable to the MFD ($d_0 \approx 5$) and α_s is chosen in a way the distance from the waveguide to the grating coupler is reduced enough $\alpha_s = 40^\circ$.

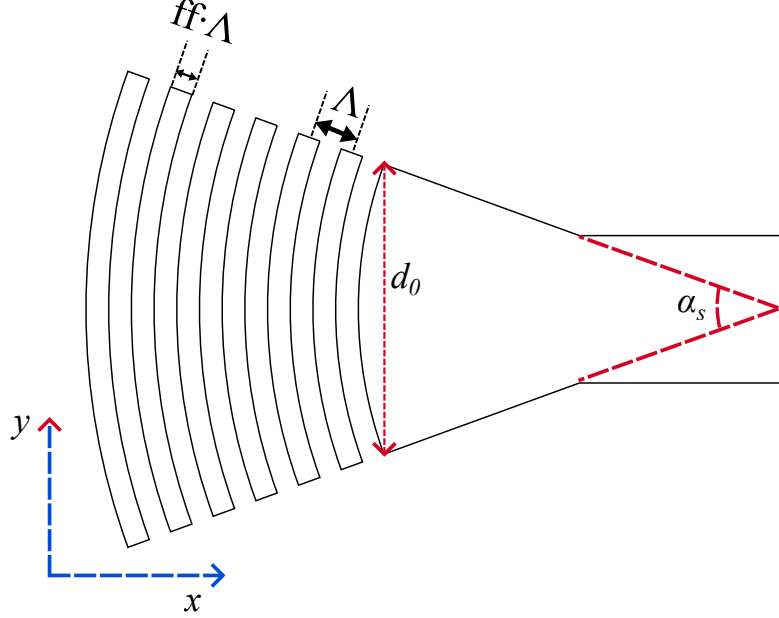


Figure 2.10: Grating coupler seen from above.

The author shows that the grating lines should follow a curvature with elliptical shapes:

$$m\lambda = n_{eff}\sqrt{x^2 + y^2} - nn_0 \sin \theta$$

Nevertheless, our design uses only concentric circles whose center is located inside the waveguide, because the real performance of the focusing grating coupler should be verified with 3D-FDTD or 3D-FEM simulations.

Finally, the number of grating lines should be high enough to cover an area the size of the incident field (this also depends on the distance from the fiber to the grating coupler). The final value is calculated in a way the sum of the all grating lines is $100\mu m$, in this way the number of grating lines is 163.

2.4 Resonant cavity

2.4.1 Definition and working principle

An optical resonator, also known as a resonant optical cavity, is a configuration of optical elements that enables light to circulate along a closed path. It can be constructed using bulk optical components or as a waveguide resonator, where light

is guided instead of being transmitted through free space. Linear resonators are designed to reflect light back and forth between two end mirrors. [14].

Resonator modes are electric field distributions that are self-reproducing in each resonator round trip. In waveguide resonators, the transverse mode structure is determined by the waveguide properties only, and is constant everywhere in the resonator if the waveguide properties remain constant. Only a single transverse mode shape can exist. For each of the transverse mode patterns, there are only certain optical frequencies for which the optical phase is self-consistently reproduced after each round trip. This means that the round-trip phase shift is an integer multiple of 2π . These frequencies are called mode frequencies or resonance frequencies and are approximately equidistant. The frequency spacing of the resonator modes, also known as Free Spectral Range (FSR), is the inverse round-trip time or more precisely, the inverse round-trip group delay. As the resonator length increases, FSR becomes smaller. The ratio of frequency spacing to resonator bandwidth (width of the resonances) is called finesse and is determined by power losses per resonator round trip. The Q factor, which is the ratio of resonance frequency and bandwidth, is a related measure.

The cavity for this project is made to have a high Quality factor in order to maximize the conversion of photons, in this way there is a higher probability of converting the RF photons to optical photons inside the waveguide.

2.4.2 Theoretical calculations

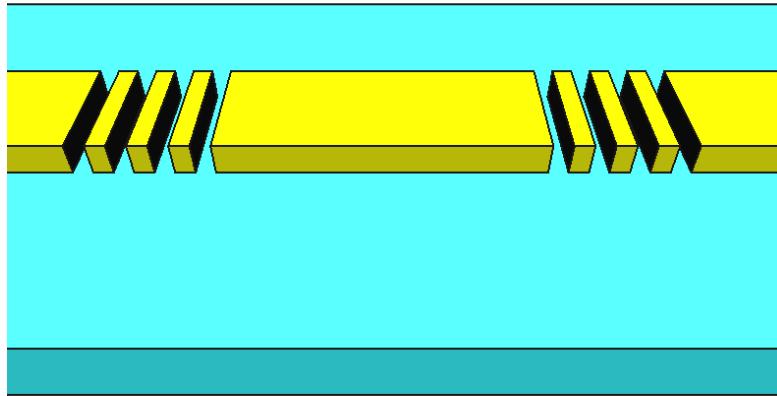


Figure 2.11: DBR resonator (simplified).

The resonator used in the design uses two Distributed Bragg Reflectors as mirrors side by side (fig 2.11), thus this is a Fabry-Perot resonator. This resonator

should satisfy the Barkhausen stability criterion, which says that the round trip magnitude should be 1 (Modulus condition) and the phase of the round trip should be an integer multiple of 2π (Phase condition) [15]:

$$|RT| = 1$$

$$\angle RT = 2m_l\pi, m_l \in \mathbb{N}$$

As seen in the figure 2.12, inside the cavity (the middle), there are two reflections when a wave is propagated inside: r_{g1} for the left Bragg mirror and r_{g2} for the right one. Assuming a cavity length $L_a = \Lambda$ (phase-shifted design), the round trip condition is accomplished for the Bragg wavelength λ_B :

$$r_{g1}(\lambda_B) \exp(-2j\beta\Lambda)r_{g2}(\lambda_B) = 1$$

$$\angle r_{g1}(\lambda_B) - 2\beta\Lambda + \angle r_{g2}(\lambda_B) = -2\frac{2\pi}{\lambda_B}n_{eff}\frac{\lambda_B}{2n_{eff}} = 2\pi = 2m\pi$$

To have a Bragg wavelength equal to the desired wavelength of ours ($\lambda = \lambda_B$), it is important to satisfy the Bragg condition in order to obtain the behavior presented in the figure 2.13 in the DBR mirrors: $\lambda_B = 2n_{eff}\Lambda$, where n_{eff} is the effective index of the grating region, calculated with the same formula used in the section of the grating coupler. Thus, the calculated period considering the previous calculations with the MATLAB code for the effective index [7] is equal to $\Lambda \approx 180nm$. Assuming a fill factor of 50%, $ff \cdot \Lambda \approx 90nm$

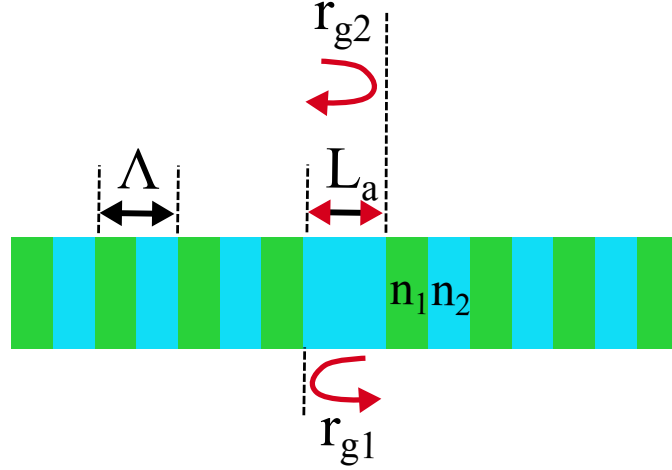


Figure 2.12: DBR resonator diagram with both reflectivities.

Finally, it is important to remark the quality factor given by the equation:

$$Q = \frac{\omega_r}{\Delta\omega} = m \frac{\pi}{1 - R}$$

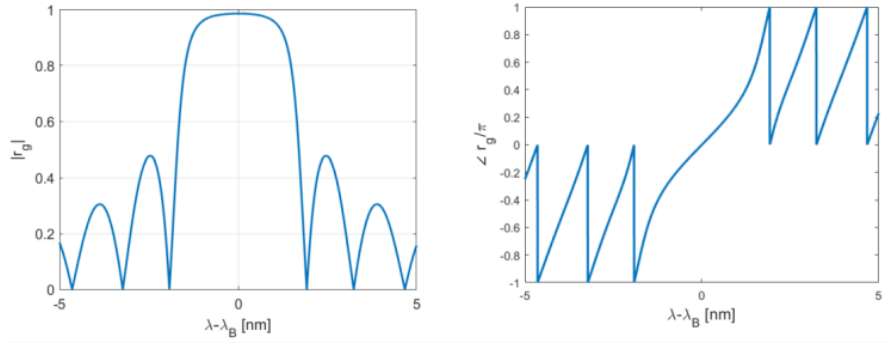


Figure 2.13: Reflectivity of the DBR mirror with respect to the differential wavelength [15]

Where ω_r is the resonant frequency, $\Delta\omega$ is the bandwidth of the resonance, m is the resonant mode and R is the reflectance of the DBR mirrors. Ideally the Q factor would be infinite for a value of $R = 1$, however in order to obtain a reflectance of 1 we would require a infinite grating. To calculate this parameter in a theoretical way, some simulations are required, something we skip in this thesis. The number of grating lines is calculated with the analytic calculation shown in the next subsection.

2.4.3 Analytic calculation

One of the methods to calculate the behavior of the Fabry-Perot resonator is using the Transfer Matrix Method (TMM), a numerical technique that is very useful for simulating the response of an arbitrary grating profile. [7]

The TMM method works as follows:

1. Calculation of reflection and transmission coefficients due to index discontinuities, and propagation coefficients for waveguide sections.
2. Representation of these building blocks as matrices, with a size of 2×2 in the case of a single-mode system.
3. Multiplication of the matrices as a cascaded network, which represents the grating.
4. Extraction of the transmission and reflection values for the overall grating. This calculation is then repeated for each wavelength.

The transfer matrix for a homogeneous section of a waveguide is:

$$T_{hw} = \begin{bmatrix} \exp(j\beta L) & 0 \\ 0 & \exp(-j\beta L) \end{bmatrix}$$

β is the complex propagation constant expressed as:

$$\beta = \frac{2\pi n_{eff}}{\lambda} - j\frac{\alpha}{2}$$

Where n_{eff} is the effective index of refraction and α is the propagation loss given by:

$$\alpha = \frac{4\pi k}{\lambda}$$

k is the imaginary coefficient in the complex index of refraction ($n + jk$).

The transfer matrix for an index of refraction step (different materials) from material 1 (air) to material 2 (SiN) is defined as:

$$T_{is12} = \begin{bmatrix} \frac{1}{t} & r \\ \frac{r}{t} & \frac{1}{t} \end{bmatrix} = \begin{bmatrix} \frac{n_1+n_2}{2\sqrt{n_1n_2}} & \frac{n_1-n_2}{2\sqrt{n_1n_2}} \\ \frac{n_1-n_2}{2\sqrt{n_1n_2}} & \frac{n_1+n_2}{2\sqrt{n_1n_2}} \end{bmatrix}$$

Where r and t are the reflection coefficients. They are based on the Fresnel coefficients (based on plane waves): this is called the "plane-wave approximation". The behavior of the Bragg grating with N periods is represented by the next cascade network:

$$T_{bragg} = (T_{hw-2}T_{is-21}T_{hw-1}T_{is-12})^N$$

Finally, the whole resonator can be thought of a cavity (homogeneous waveguide with length $L = \Lambda$) and 2 Bragg reflectors:

$$T = T_{bragg}T_{hw-3}T_{bragg}T_{hw-3}$$

Where 3 is the same material as 2 (SiN) but with different waveguide length as shown in figure 2.14.



Figure 2.14: Material numbers for the optical resonator

When implementing a code in MATLAB with the previous matrices [7], the results of transmission and reflection for different number of grating lines is shown on figure 2.15. From these results it can be seen that when increasing the number of grating lines, the Q factor of the resonance frequency is noticeably increased, thus the bandwidth is also decreased. For the purposes of this project, the initial Q value should be at least $Q = 20$, thus the selected number of grating periods should be at least 2.

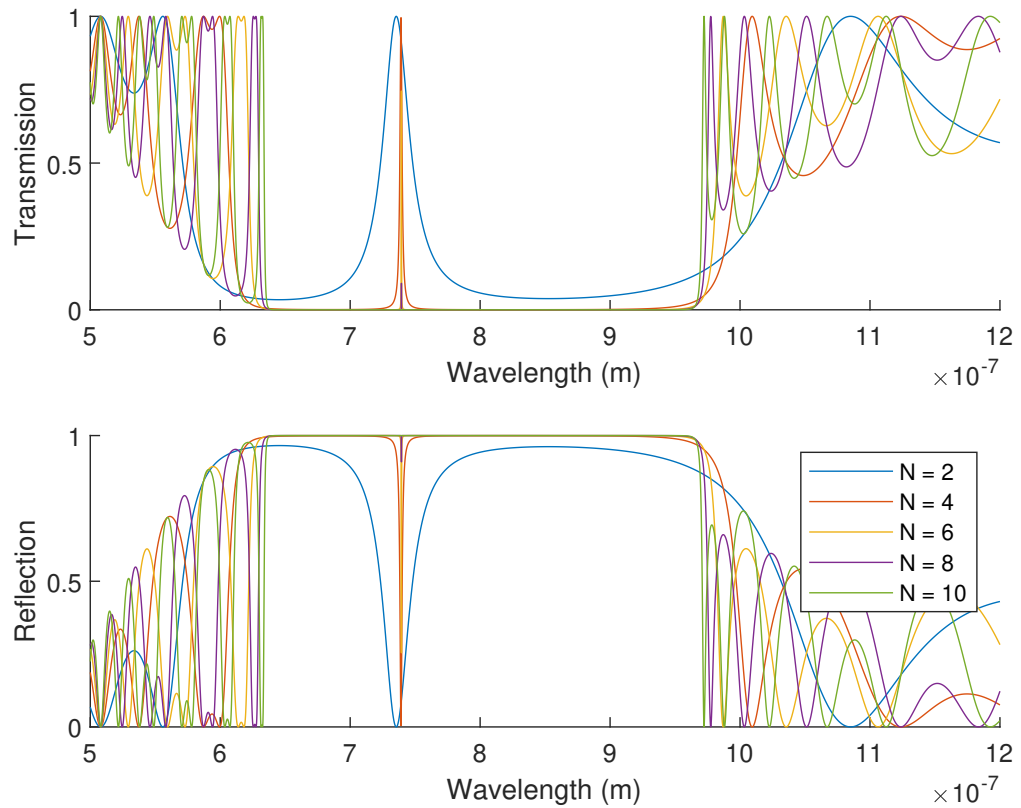


Figure 2.15: Results for TMM simulation with MATLAB for different number of grating periods going from 2 to 10. This simulation is done without considering the propagation losses ($\alpha = 0$)

Chapter 3

Material Deposition and Characterization

3.1 Chemical Vapor Deposition

3.1.1 Description of CVD

Chemical Vapor Deposition (CVD) is a process that creates thin films from gaseous precursors. The films can be made of metals, semiconductors, or insulators and are used in the manufacturing of microelectronic devices. The most common process conditions are high temperatures and low pressures. It's important to note that an energy source is required to break the gaseous precursors into reactive species for deposition. [16] The steps involved in the CVD process are :

1. Vaporization and transport of precursor molecules into a reactor
2. Diffusion of precursor molecules to the surface of the substrate
3. Adsorption of precursor molecules to the surface and further diffusion across the surface. This is temperature dependent and affects step coverage
4. Decomposition of precursor molecules and incorporation into solid films
5. Desorption of volatile byproducts into the gas phase

The reaction rate strongly dependent on the temperature, according to the following formula:

$$R = R_o \exp\left(-\frac{E_a}{kT}\right)$$

Where R_o is the frequency factor, E_a is the activation energy, k is the Boltzmann constant and T is the Temperature. Thus, the surface reaction rate increases with

increasing temperature and saturates to a maximum (R_o) at very high temperatures. Therefore, at high temperatures the process is mass-transport limited while at low temperatures is reaction rate limited.

The acceptance angle and conformality are important factors to consider. The growth rate depends on the flux density of gas molecules that hit the surface, which is determined by the acceptance angle. However, in the case of our sample, which only requires a thin film deposition of Silicon Nitride, these factors are not relevant to the fabrication process.

In Plasma Enhanced CVD (PECVD), a plasma is created using an RF voltage. The plasma contains electrons, ionized molecules, neutral molecules, neutral and ionized fragments of broken-up molecules, excited molecules, and free radicals. Free radicals are neutral species that have incomplete bonding and are highly reactive.

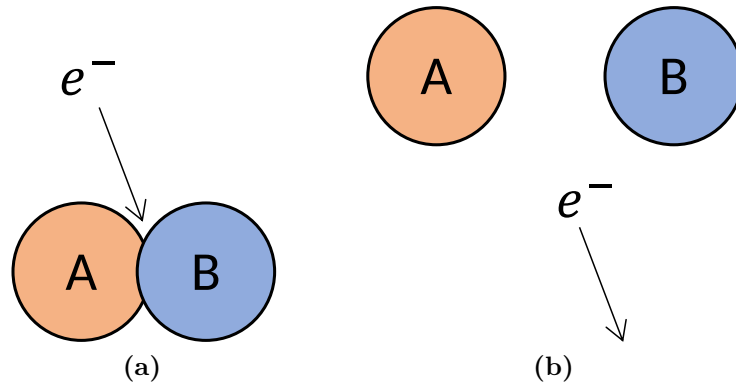


Figure 3.1: Dissociation process for the generation of strongly reactive free radicals: (a) Electron colliding to a molecule. (b) Free radicals generation.

The combination of fragmentation, free radicals, and ion bombardment enables surface processes and deposition to take place at significantly lower temperatures compared to a typical CVD system. Plasmas are employed to drive reactions that would otherwise be impossible at low temperatures, as plasma serves as the energy source that generates reactive gases.

The following are the control parameters for PECVD:

1. Temperature
2. Deposition time
3. Gas composition (precursors) and flow rate
4. System pressure and reactant partial pressure
5. RF power, frequency, and bias

In our situation, we employ an Inductively Coupled Plasma CVD (ICP-CVD) system from Oxford [17]. The plasma is generated by a plasma source, and the energy is supplied by electric currents produced through electromagnetic induction, specifically, by time-varying magnetic fields. [18]

3.1.2 Parameters to increase the refractive index

ICP-CVD offers a great advantage for low-temperature processing over PECVD. Considering the paper by J.W.Lee et al [19] they achieve Silicon Nitride deposition at low temperature with two different gas chemistries: $\text{SiH}_4/\text{N}_2/\text{Ar}$ and $\text{SiH}_4/\text{NH}_3/\text{He}$. Because N_2 has a relatively low dissociation efficiency, Silicon Nitride deposition recipes in PECVD typically employ NH_3 as the nitrogen source. Therefore, hydrogen incorporation from NH_3 into deposited SiN_x is unavoidable. However, high-density plasma CVD allows us to deposit SiN_x without the need for NH_3 because high-density plasma sources generally exhibit higher ion dissociation efficiency. The author shows that a high refractive index ($n \approx 2.4$) can be achieved at a chamber pressure of around 20 mTorr.

In our work we use the first gas mixture ($\text{SiH}_4/\text{N}_2/\text{Ar}$) as it is suitable for the available gases. First, the surface is functionalized using Nitrogen plasma only to improve the adhesion: this process has a duration of 1 min and the flow rate of N_2 is set at 20sccm. Then the plasma is deposited with a plasma mixture of the gases shown in the table 3.1, to reach a final pressure of 20 mTorr. Since the deposition machine has an internal offset, the flux of N_2 is set to 14.7 sccm instead of 13. The RF power is set at 120W, and the ICP power at 800W. Finally, the carrier used for the deposition is a Silicon wafer pre-covered with SiN (3 minutes) before the first deposition, this one is kept the same for all the samples. An example of a deposited sample is shown in the figure 3.2, where the Silicon Nitride gives the sample a yellowish color.

Gas	Flow rate (sccm)
N_2	9
Ar	20
SiH_4	13

Table 3.1: Gas flow rates for Silicon Nitride deposition

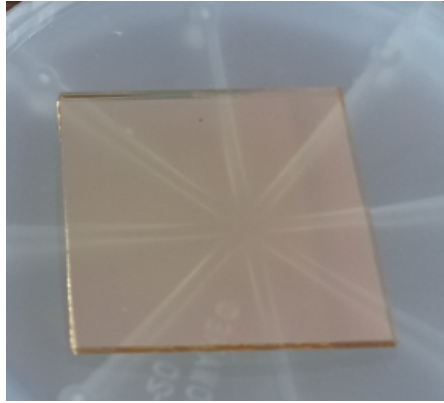


Figure 3.2: A sample of corning glass with a layer of Silicon Nitride above

3.2 Ellipsometry

3.2.1 Description

Ellipsometry is an optical technique that measures the change in polarization of light as it reflects or transmits from a material structure. This change is represented as an amplitude ratio Ψ and the phase difference Δ . The measured response depends on the optical properties and thickness of individual materials. Therefore, ellipsometry is primarily used to determine film thickness and optical constants such as the refractive index. However, it can also be used to characterize other material properties such as composition, crystallinity, roughness, doping concentration, and other properties associated with a change in optical response [20]. A diagram of how the light is reflected in the sample is shown in the figure 3.3.

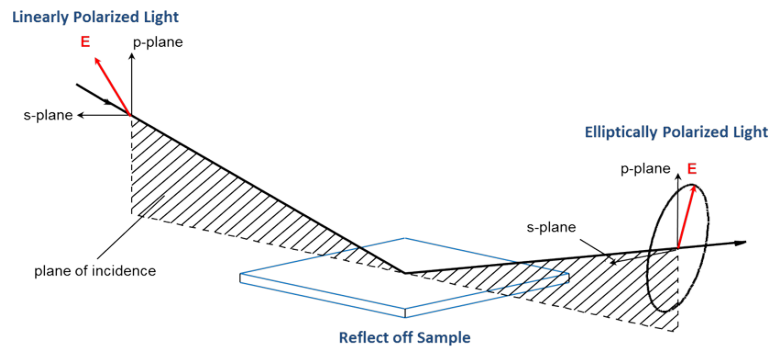


Figure 3.3: Diagram of the working principle of Ellipsometry [20]

For the analysis of the SiN layer we used an ellipsometer capable of measuring at different angles (65.13° , 70.14° and 75.14°). We employed Cauchy's analysis

to determine the optical constants of a transparent or partially transparent film (Dielectrics and Semiconductors below the fundamental bandgap). Over a portion of the spectral range, the optical constants of these materials can be represented by an index that varies slowly as a function of wavelength λ and an exponential absorption tail. The index of refraction of the Cauchy layer is represented by an inverse power series containing only even terms [21]:

$$n(\lambda) = A + \frac{B}{\lambda^2} + \frac{C^4}{\lambda}$$

Where A, B and C are variable fit parameters that determine the index dispersion. The extinction coefficient is represented by a simple exponential tail describing an Urbach absorption tail:

$$k = k_{amp} \cdot \exp(e_{xp}(E - E_{band-edge}))$$

Where k_{amp} and e_{xp} are fit parameters for determining the shape of the extinction coefficient dispersion. E is the photon energy in eV and $E_{band-edge}$ parameter can be set manually.

3.2.2 Results

All the samples were measured with the ellipsometer with the purpose of acquiring the refractive index and the thickness of the SiN layer (in order to calculate the deposition rate). An example of a plot of the acquired data is present in the figure 3.4, while the optical constants calculated with the Cauchy's model is shown in the figure 3.5

The thicknesses vs deposition time of the samples is shown in the figure 3.6. The linear fit for the thickness with respect to deposition time is:

$$t = 37.07\tau_{dep} + 8.49$$

Where t is the thickness and τ_{dep} is the deposition time

3.3 Optical Profilometry

3.3.1 Description

Optical profilometry is a non-contact technique employed to examine the topography of a surface. Unlike physical probes like Stylus Profilers, this method relies on light to gather data. It involves directing a light source towards the surface to capture its three-dimensional data. Various light-based techniques, such as optical

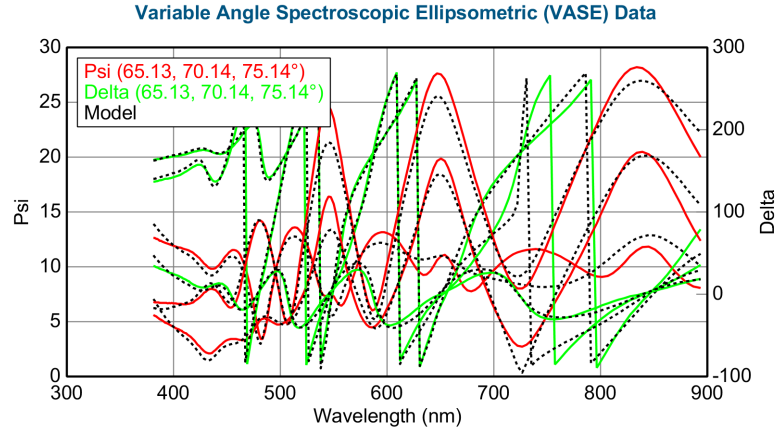


Figure 3.4: Plot of amplitude ratio Ψ , and the phase difference Δ with respect to the wavelength in nm of one of the SiN samples. The Cauchy model has been used for the model fitting

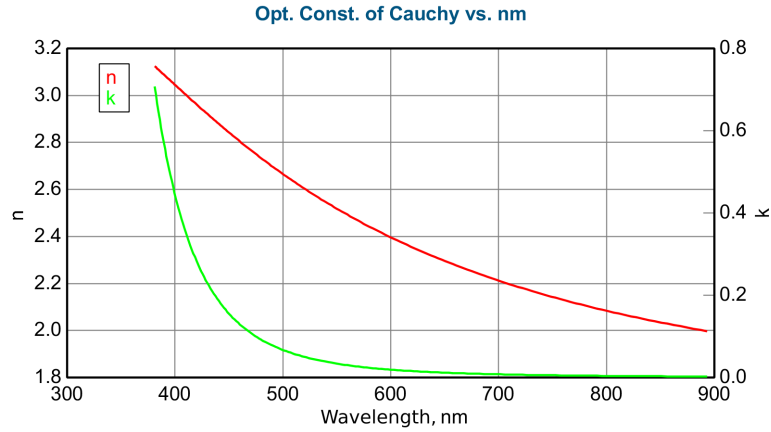


Figure 3.5: Plot of real refractive index (n) and the extinction coefficient (k) with respect to the photon wavelength in nm

interference, focus and phase detection, and confocal aperture detection, are used to measure the surface profile. [22]

Optical profilometry works in such way to not destroy neither touch the surface. The light from the profiler lamp is split into two paths by a beam splitter. One path is directed towards the surface, while the other path is directed towards the reference mirror (fig 3.7). The two paths of light reflected from the surface and the reference mirror are combined and projected onto an array detector. The difference in the path of the recombined beams is on the order of a few wavelengths, which results in minimal interference.

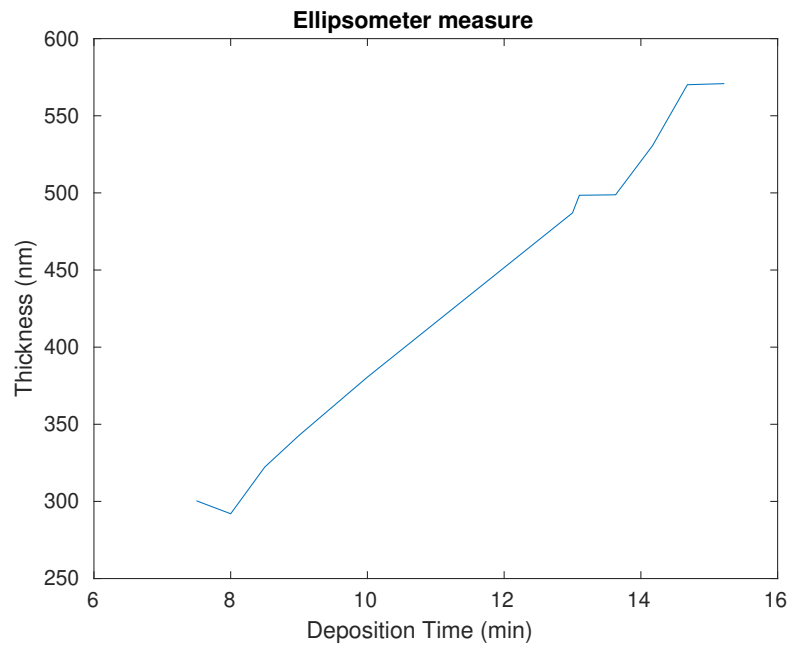


Figure 3.6: Plot of thickness vs deposition time with data from the ellipsometer

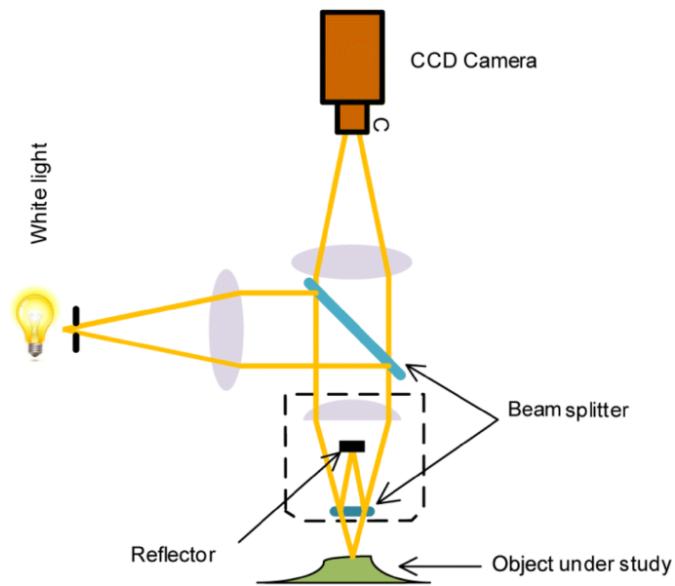


Figure 3.7: Working principle of optical profilometer. [23]

The following are the key performance factors to consider when using optical profilometry:

1. Spatial resolution: This parameter varies across different profilometers, mainly

in the longitudinal and lateral directions. The range of this parameter depends on the users' objectives, which in turn depend on the desired accuracy levels.

2. The field of view (FOV): This parameter refers to the total area of the material surface that can be measured by the profilometer. It is important for understanding the properties of a larger area and depends on the type and size of the profiler.
3. Image acquisition time: This parameter depends on the measuring method, the type of image required, image frame rates, and accuracy.

The key advantage of this profilometer is its non-contact mode of operation, which utilizes a light source to analyze the surface of the material. This enables true imaging, allowing for area measurements to be obtained. Compared to contact mode, data acquisition with this profilometer is high-speed, and large areas can be sampled. The technique enables critical dimensional measurements, including the x, y, and z coordinates, facilitating the acquisition of three-dimensional surface data.

In our work, the profilometer is used to characterize the surface profile of our samples, and in this section is used to measure the thickness of the material. Before the deposition of SiN into the corning glass, we put a tape at one corner, then after the deposition we remove the tape in order to strip the material at the corner. In this way we can measure height of the step with the profilometer.

3.3.2 Results

When measuring the sample with the profilometer, the program allow us to take a 1D profile of the sample. An example of the data acquired is shown in the figure 3.8. The thicknesses vs deposition time of the samples is shown in the figure 3.9. The linear fit for the thickness with respect to deposition time is:

$$t = 39.16\tau_{dep} + 8.72$$

3.4 Stylus Profilometry

3.4.1 Description

Stylus profilometry is a method of measuring the surface topography of a sample. It involves physically moving a probe along the surface to detect its height. The probe is in direct contact with the surface and traces the desired path to determine the topography of the surface. The changes in the Z position of the arm holder can then be used to reconstruct the surface. This technique is highly sensitive

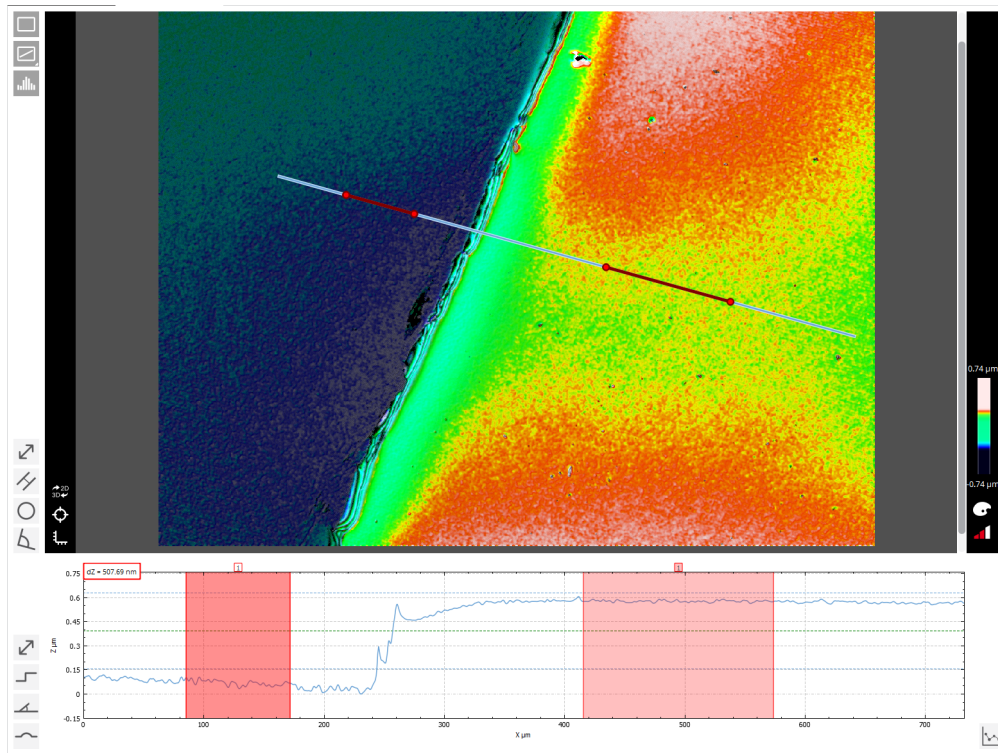


Figure 3.8: Measurement of the step height at the corner of one sample with optical profilometer

and provides high Z resolution, but it is sensitive to soft surfaces and can damage them. Additionally, the probe can become contaminated by the surface, which could affect the accuracy of the measurement. [24]

3.4.2 Results

The measurement is done in the same position as the optical profilometer one (at the corner). Then the results are given by a thickness profile vs distance on x as seen in the figure 3.10. The thicknesses vs deposition time of the samples is shown in the figure 3.11. The linear fit for the thickness with respect to deposition time is:

$$t = 40.43\tau_{dep} - 35.78$$

3.5 Deposition rate comparison

Analysing the 3 linear regression of the material thickness in the deposition, the slope of each one doesn't differs too much, meaning that the analysis with all the

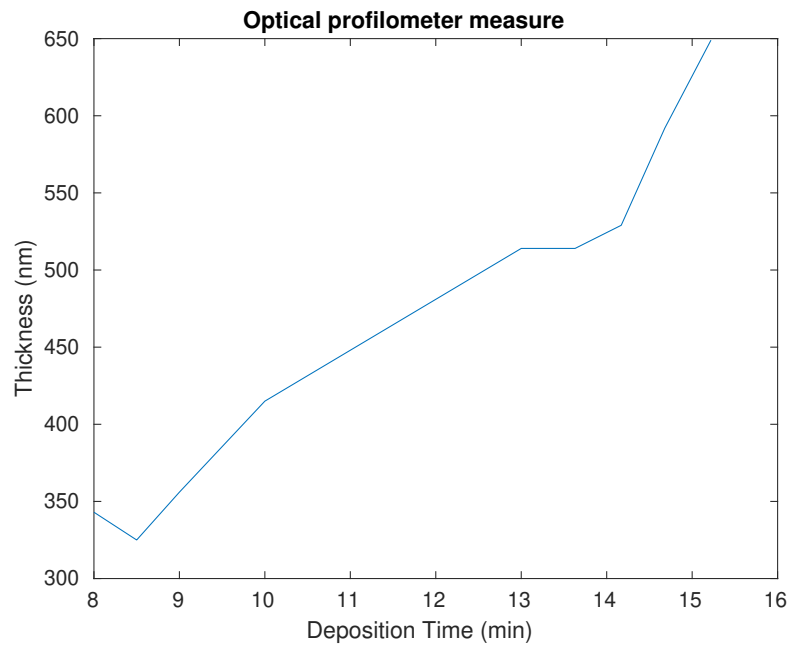


Figure 3.9: Plot of thickness vs deposition time with data from the optical profilometer

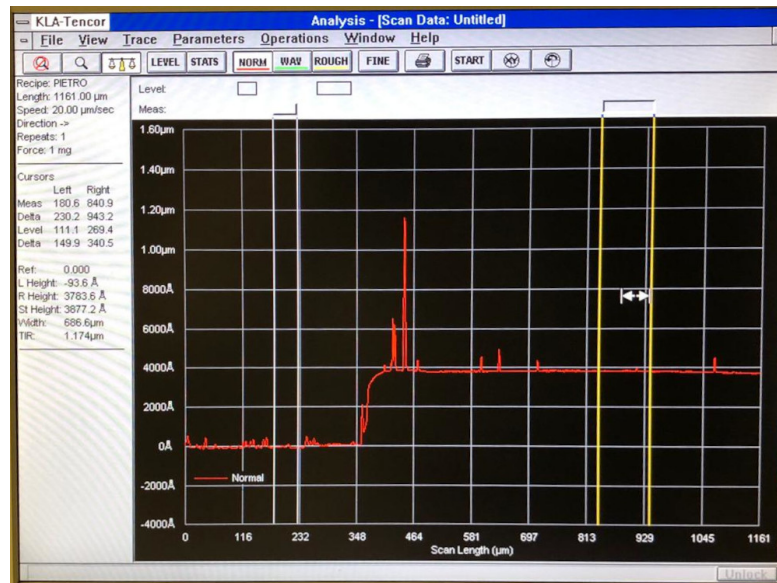


Figure 3.10: Plot of thickness vs position on x

three instruments was correct. One way of calculating the "real" thickness function

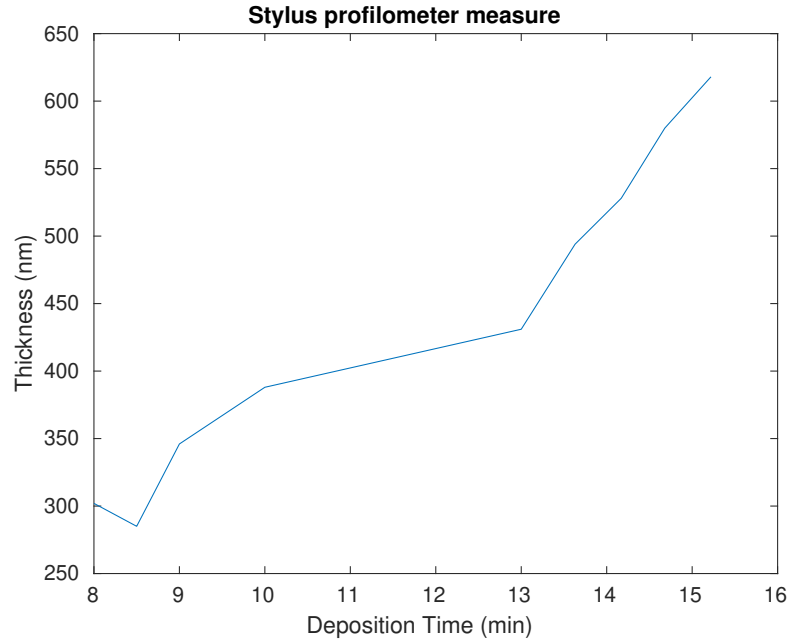


Figure 3.11: Plot of thickness vs position on x

would be to average the three terms:

$$t_{av} = \frac{t_1 + t_2 + t_3}{3} = 38.89\tau_{dep} - 6.1929$$

Meaning that the deposition rate is 38.89 nm/min with an offset of -6.1929 nm. This is only a model for our deposition model assuming that is a linear one and not taking into account the error put on the measures, since a negative value of thickness does not make sense.

3.6 X-ray Photoelectron Spectroscopy

3.6.1 Description

X-ray Photoelectron Spectroscopy (XPS) is a non-destructive technique that enables the analysis of the outermost layers (approximately 10nm or 30 atomic layers) of both natural and engineered materials. It provides valuable insights into the composition of material surfaces, including the presence of specific elements, the relative abundances of these components, and the chemical state of polyvalent ions. This is achieved by measuring the binding energies of elements, which are indicative of the nature and strength of their chemical bonds. XPS is widely employed to

characterize a diverse range of materials, including inorganic compounds, organic compounds, semiconductors, thin films, and coatings. [25]

XPS utilizes the photoelectric effect, as described by Einstein. It involves the emission of electrons from atoms when they are exposed to electromagnetic radiation. According to Einstein's prediction, photoelectrons are generated when the energy of the impinging photons surpasses the binding energy of electrons in the material. The kinetic energy of an emitted electron is directly associated with the binding energy of each electron:

$$E_{kinetic} = E_{photon} - E_{binding} - \phi = hv - E_{binding} - \phi$$

Where ϕ is the work function of the solid, h is the Planck's constant and v is the photon's frequency.

The technique is a non-destructive technique, however, if the analysis requires information about the volume of the material, an Ar ion gun can be used to sputter the surface. This process removes environmental contaminants from the surface and allows for depth profiles to be obtained across surface layers.

3.6.2 Material Composition

We analyzed the deposited sample with SiN using this technique and the results are shown in the figure 3.12. From this results, we can see that the SiN is non stoichiometric since it has a higher concentration of Silicon (around 64%) than Nitrogen (around 36%), this, for etching this material we would need a different recipe that is more adapted to etch Silicon. It is possible to see that we arrive at the interface when the Oxygen is increased and the Nitrogen is decreasing. At this point the sputtering has arrived to the corning glass, that is why Oxygen, Silicon and Barium are present.

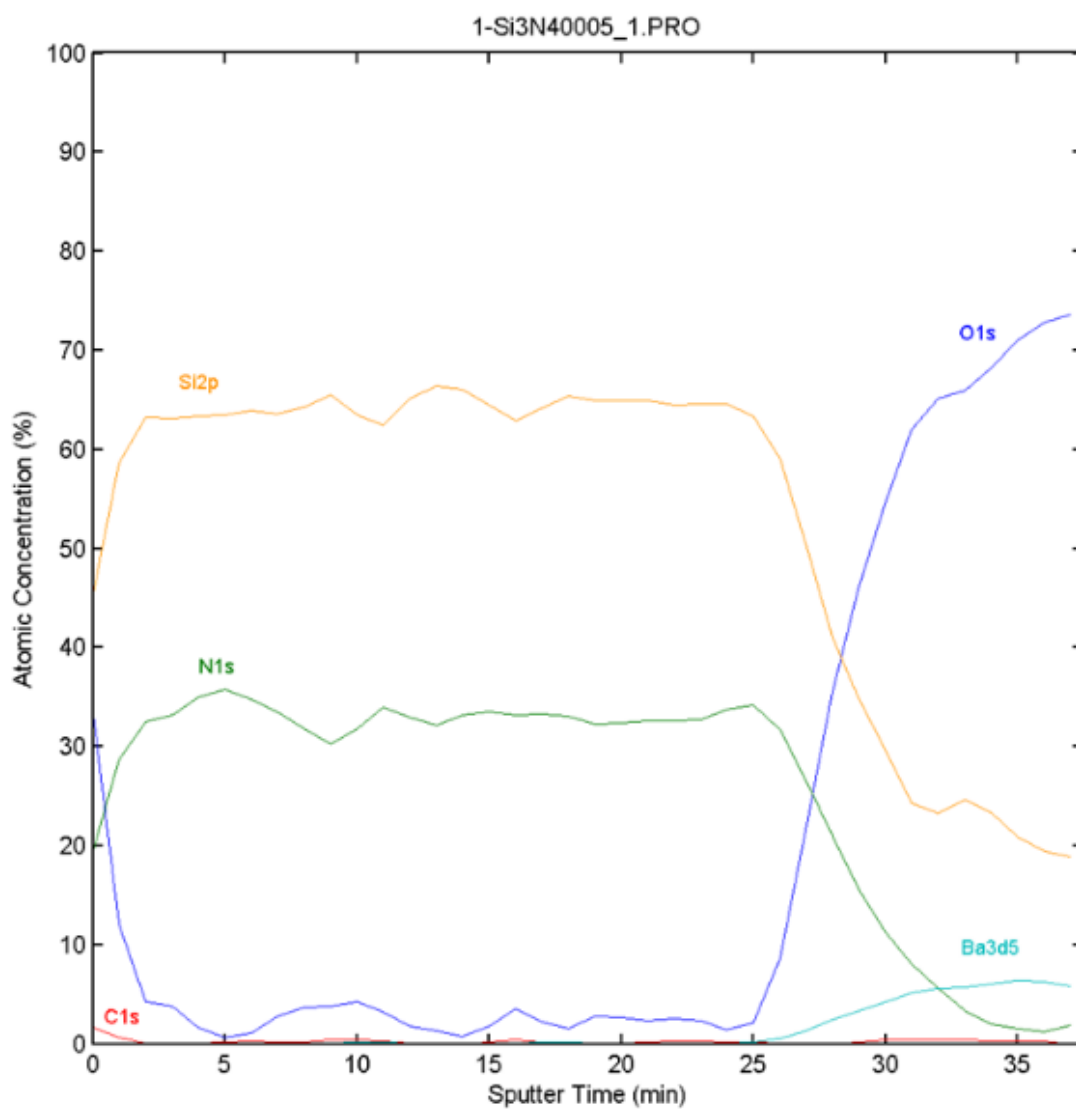


Figure 3.12: XPS results

Chapter 4

Lithography

4.1 Optical Lithography

4.1.1 Description

Optical Lithography, also known as Photolithography, is a method employed to transfer a desired pattern from a master copy (or mask) onto a polymer layer (referred to as photoresist) on the wafer surface. For instance, when fabricating a circuit, photolithography is utilized to transfer the circuit element patterns required for the construction of semiconductor devices.

A mask can be used to cover some zones from the light to transfer the pattern, and depending on the nature of the photoresist (positive or negative), the exposed zones are removed or remain when the resist is developed [16].

For this work, the lithographic process was performed with a maskless system, the *Heidelberg μ PG 101* which is a micro pattern generator for direct writing applications and low volume mask making. Its laser wavelength is 405nm. The photosensitive coating of the substrates has to be chosen according to the wavelength used and the intended application [26]. For this process to work, a CAD must be designed before starting the photolithography with the machine. This kind of system allows great flexibility, as there are no physical masks; the drawback is the time required to perform the lithography since for big structures a larger area is covered.

The standard lithographic process (fig 4.1) begins with the cleaning of the substrate. In this case, since the substrate has a previous deposition of Silicon Nitride, there is no problem with the cleaning process. Acetone is typically used as a solvent to clean the substrate. The sample is then placed inside a warm ultrasonic bath and immersed in ethanol. Acetone is used to remove organic contaminants from the surface, while ethanol is used to prevent any remaining residuals after cleaning with acetone. This is done because acetone evaporates at a high rate.

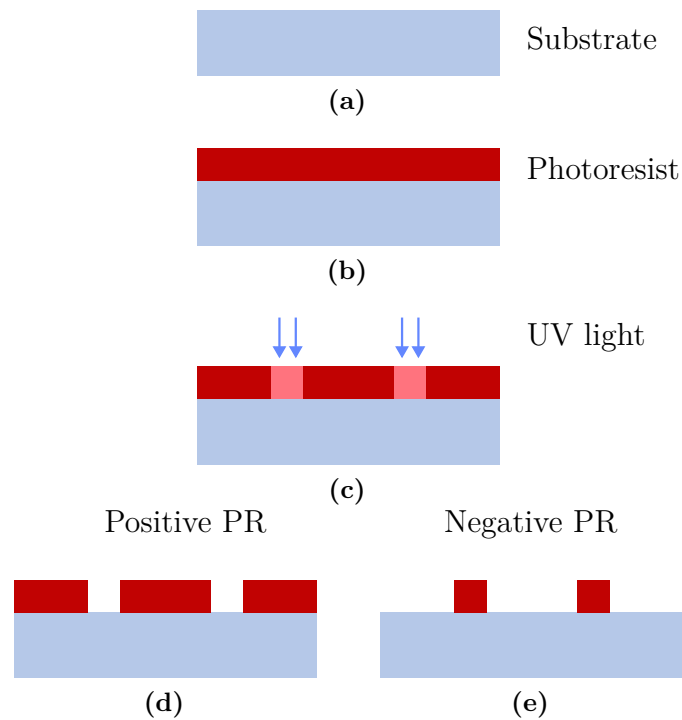


Figure 4.1: General photolithographic process: (a) Cleaning of the substrate. (b) Substrate after the spin of the resist on it. (c) Exposure of the zones for the pattern transfer onto the resist. (d) Result after developing if the resist is a positive PR. (e) Result after developing if the resist is a negative PR.

Finally, the substrate is dried with N_2 . This cleaning step is crucial to prevent contaminants from remaining on the substrate, which could lead to poor adhesion of the photoresist or unwanted masking of certain areas. Once the substrate is cleaned, the photoresist solution is applied using a spin-coating technique. This process ensures that a precise thickness of the resin is uniformly deposited onto the substrate's surface. The desired thickness can be achieved by adjusting the angular velocity and time parameters. Typically, resist manufacturers provide datasheets with curves, such as Thickness vs RPM, to help customers select the optimal parameters for achieving the desired thickness.

After the photoresist has been deposited onto the surface, a soft bake step is performed to ensure the complete evaporation of all solvents and the stabilization of the resist. It is crucial to maintain a constant temperature throughout the entire baking process.

Now that the wafer is ready for the exposure, it is placed in the laser writer to transfer the pattern of our CAD. Next, when the writing has finished, the substrate is immersed in a developing solution (in our case the AZ DEV which is a positive

resist developer)

PR are photosensitive organic mixtures which contain mainly:

1. Inactive polymer resins, which is a binder that proved mechanical and chemical properties. Useful for adhesion, chemical resistance, rigidity, thermal stability, etc.
2. PhotoActive Compounds (PAC)
3. A solvent, which controls the viscosity of the base, keeping it in liquid state for the spinning phase. This affects the thickness

In the developing phase, there are two outcomes depending on the nature of the resist. The PR can be:

1. Photons break the polymer chains, making them more soluble in the developing solution. Consequently, when a zone is exposed to light, the photoresist (PR) in that zone is removed after development.
2. Photons induce cross-linking of the polymer chains, making them less soluble in the developing solution. This results in the inverse pattern of the design being replicated onto the wafer. In other words, after development, the zones where light has not impinged are removed.

The recipe used for the photolithography process is:

1. Cleaning of the sample with acetone (with ultrasound) and ethanol.
2. Spin-coating of the resist (AZ5214E: positive PR) into the sample surface at 3500 RPM for 30 seconds.
3. Pre-baking of the sample at 110° for 3 minutes.
4. After the exposure, developing of the sample with AZ DEV and deionized water (proportions of 1:1) for 25 seconds.

4.1.2 Test designs

To test the quality of the lithography we made a design with of circles and squares of different dimensions. Going from $50\mu m$ to $10\mu m$. The result of the lithography can be seen in the figure 4.2. Another lithography was made with structures having dimensions from $50\mu m$ to $0.5\mu m$ and it was possible to observe that the structures with lower dimensions got rounded at the corners, giving us a look of which is the limit for the laser writer. This lithography will be used after for the etching tests of the material.

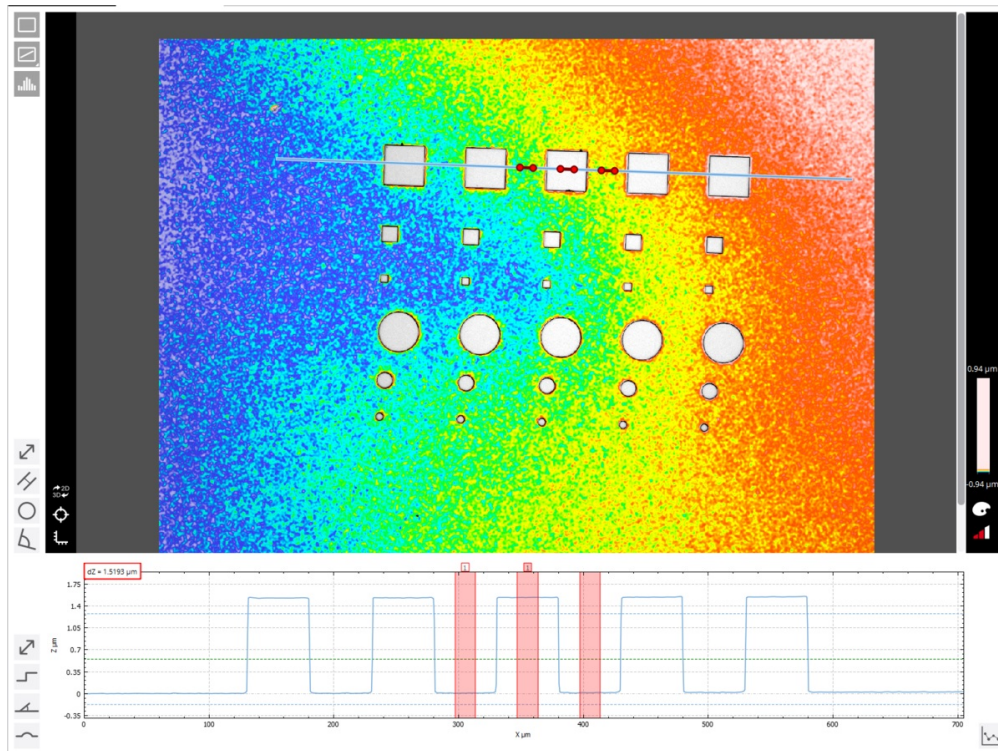


Figure 4.2: Photolithography test after developing. Measured with Optical profilometer. It can be seen that the height of the resist is around $1.5\mu m$

4.2 Sputter Deposition

4.2.1 Description

Sputtering is a method of Physical Vapor Deposition (PVD) that involves the condensation of a vapor onto a cooler substrate to achieve film growth. PVD can also be achieved through evaporation. Compared to evaporation, sputtering has better step coverage, which results in better conformality [16].

This technique involves the use of plasma to dislodge atoms from a target material, which then deposit on wafers to form a film. The process is based on ion bombardment, and Ar^+ is typically used as the sputtering gas. Compared to evaporation, sputtering requires higher pressures, which can lead to greater contamination. However, sputtering has excellent adhesion properties, and it is possible to perform an in-situ cleaning prior to film deposition.

The most straightforward method of sputtering involves placing a target material in the cathode (negative potential) within a vacuum chamber. The target undergoes erosion, and the material is subsequently deposited on the substrate positioned at

the anode (positive potential). A high voltage of 100 Volts is applied between the plates to initiate plasma discharge and facilitate the acceleration of positive ions towards the target (fig 4.3). The plasma consists of approximately equal quantities of positive argon ions, electrons, and neutral argon atoms.

The steps for the process are:

1. Argon ions are accelerated across the cathode sheath to the negatively charge cathode, striking the target
2. Atoms are sputtered due to the collision.
3. The sputtered atoms travel through the plasma and are deposited on the wafers sitting on the anode.

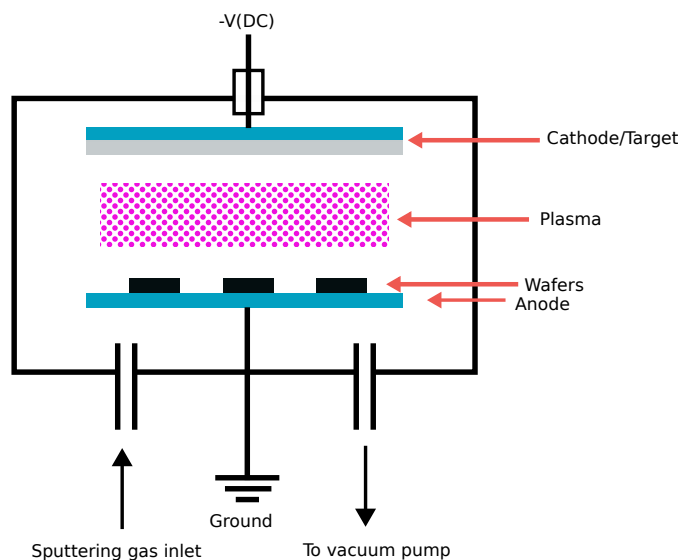


Figure 4.3: Sputtering deposition chamber with all the component

To prepare for a sputter deposition process, the same equipment is used to perform sputter etching. Sputter etching is carried out when it is necessary to cleanse the surface (e.g., after a previous photolithography process to remove the bottom resist before metal deposition) or to enhance the sample's roughness. In this scenario, the substrate assumes the role of the target, resulting in a highly anisotropic dry etching.

4.2.2 Used recipe

For sputter etching the used parameters are:

1. Pressure: $4 \cdot 10^{-2} \text{mbar}$
2. Power: 25W
3. Bias Voltage: 670V
4. Time: 2 minutes

Then, for the deposition of Aluminum:

1. Pressure: $5 \cdot 10^{-3} \text{mbar}$
2. Power: 0.13kW
3. Bias Voltage: 427V
4. Current: 0.31A
5. Pre-sputtering time: 5 minutes
6. Sputtering time: 60 seconds

The previous parameters give us a deposition rate of 0.5nm/s .

4.2.3 Lift off

After the lithography step, the lift-off process is carried out. Once the resist has been developed, a film is deposited. Some parts of the film will be over the resist and some others over the substrate. This is done to pattern the inverse design of the patterned PR with another material. For instance, it can be used to pattern a design with Aluminum, which can be used as a hard mask for an etching process. The lift-off process is illustrated in figure 4.4. In our case, we used the lift-off process to pattern a hard mask made of Aluminum and Gold.

When performing lift-off, it is crucial to ensure that the thickness of the film is less than that of the resist. Typically, the maximum thickness of the film is one-third of the resist thickness. This is done to ensure that there are no connections between the top and bottom of the film and to guarantee good striping of the structures. The lift-off process yields better results when Image Reversal resists with negative slope are used (fig 4.5) [16].

For our work, sputtering is used to deposit the hard mask in the photolithography done before, in a way we are able to do a lift off of the structure to obtain a hard mask which is used for the etching tests of SiN.

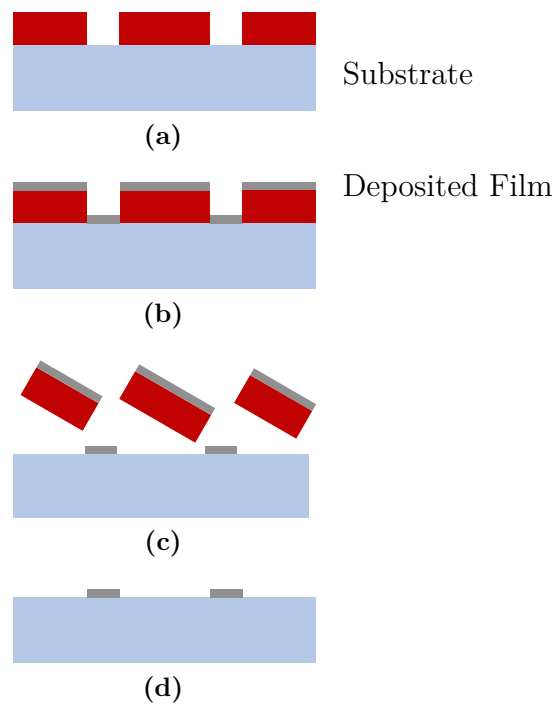


Figure 4.4: General lift-off process: (a) Initial substrate. (b) Deposition of film into the substrate. (c) Insertion of substrate into solvent for lift-off. (d) Final substrate without the PR.

4.3 Scanning Electron Microscopy

4.3.1 Description

The scanning electron microscope (SEM) employs a focused beam of high-energy electrons to produce a range of signals at the surface of solid specimens. These signals, which arise from interactions between electrons and the sample, provide insights into various aspects of the sample, such as its external morphology, chemical composition, and crystalline structure. They also reveal details about the orientation of materials constituting the sample. [27]

Accelerated electrons in a SEM carry significant amounts of kinetic energy. When these electrons are decelerated in the solid sample, they release this energy as a variety of signals produced by electron-sample interactions. The signals include secondary electrons (SE), backscattered electrons (BSE), diffracted backscattered electrons (EBSD) (used for crystal structures and mineral orientations), photons, visible light, and heat. Secondary electrons are commonly used to visualize morphology and topography on samples, while backscattered electrons are valuable for illustrating contrasts in composition in multiphase samples.

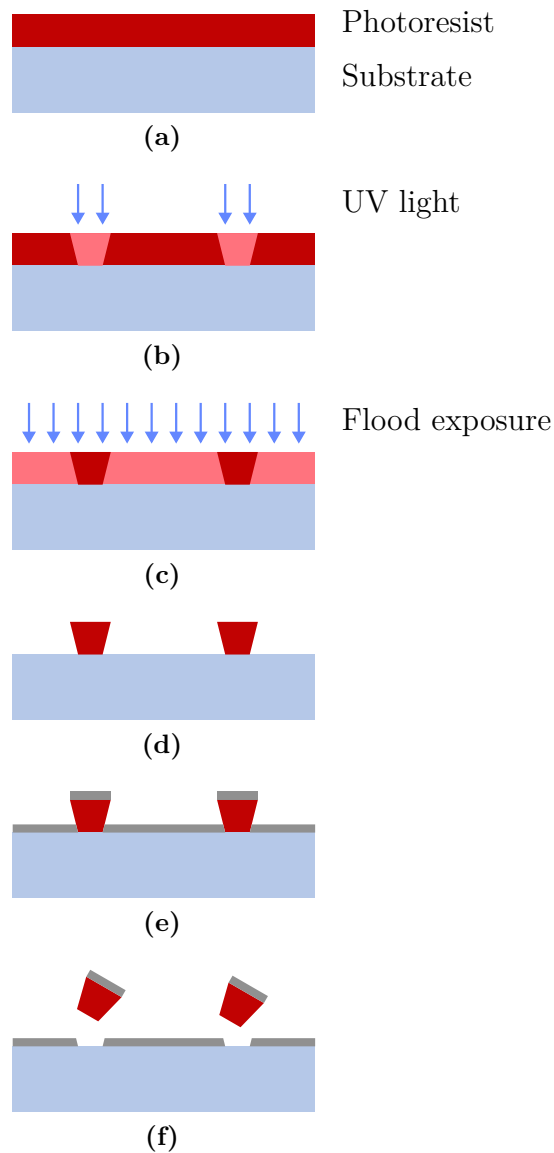


Figure 4.5: General lift-off process with image reversal: (a) Initial substrate with resist. (b) Exposure of the zones for the pattern transfer onto the resist. (c) Reversal bake to crosslink the previously exposed area. After the bake, flood exposure of the hole surface. (d) Development of the sample. (e) Deposition of film. (f) Lift-off with solvent.

The SEM has certain limitations. Firstly, it can only analyze solid samples that fit within the microscope chamber. Samples that are prone to outgassing at low pressures or are made of dielectric materials are not suitable for examination using conventional SEMs. However, there are also “low vacuum” and “environmental”

SEMs available. Our microscope is capable of seamlessly switching between high and low vacuum modes.

4.4 Electron Beam Lithography

4.4.1 Description

Instead of using photons to radiate the resist, this technique employs electrons. Electrons exhibit wave-like properties with wavelengths ranging from 0.2 to 0.5 Å, where diffraction is negligible. Unlike photolithography, this method allows for the creation of nanometric-scale features without requiring a mask. The machines responsible for electron beam lithography (EBL) are highly automated and offer precise control. Simultaneous feature detection enables extremely accurate alignment. Economic systems, such as the one employed by INRIM, are derived from scanning electron microscopes. [16]

PMMA is the most commonly used positive resist, enabling high resolution and suitable for wavelengths below 240 nm (deep UV, extreme UV, electron-beam lithography, X-ray lithography). However, for this project, a negative resist is employed: ma-n 2405 (500 nm thickness) and ma-n 2401 (100 nm thickness). These two resists serve as masks for etching the Silicon Nitride of the substrate, with the exposed zones remaining as masks. Additionally, Omnicoat is applied before spin-coating the substrate to enhance adhesion of the resist to the Silicon Nitride surface and facilitate easy stripping of the resist after subsequent processes [28].

The electron beam exposure methods can be classified into two types:

1. Raster scan: The E-beam passes over every position of the mask and is deactivated where exposure is not required.
2. Vector scan: The E-beam only passes over positions of the mask where exposure is required and jumps from one feature to the next. This method is faster than raster scan.

For which the usual doses used in the process are in the range of 1 to $100\mu C/cm^2$. The dose is calculated as:

$$Dose = \frac{Current \cdot time}{area}$$

In our case, as we are doing a lithography above SiN (dielectric material), it is better for us to work in low vacuum conditions for the EBL lithography, since we don't want to charge up the sample and ruin the lithography.

The used recipe for the EBL lithography is:

1. Cleaning of the substrate with acetone (with ultrasound) and ethanol.

2. Spin-coating of OmniCoat at 500 RPM for 5 seconds in the first cycle and 3000 RPM for 30 seconds in the second cycle.
3. Baking of the sample at 200° for 1 minute
4. Spin-coating of ma-n2405 at 3000 RPM for 30 seconds
5. Baking of the sample at 90° for 1 minute and 30 seconds
6. After the exposure, developing of the sample with the developer ma-D525 for 55 seconds

4.4.2 NPGS software

The Nanometer Pattern Generation System (NPGS) is the most popular scanning electron microscope (SEM) lithography system among research institutions in North America, and its adoption has spread worldwide. The primary goal of NPGS is to offer a robust and user-friendly system for performing advanced electron beam lithography (EBL) or ion beam lithography using a commercial SEM, STEM (Scanning Transmission Electron Microscope), FIB (Focused Ion Beam), and other related technologies. [29]

NPGS enables users to document their designs in a highly organized manner. The NPGS software facilitates the creation of personalized batches tailored to specific requirements. This approach allows for lithography with varying exposure doses, enabling the identification of optimal conditions for achieving relatively high-quality structures.

4.4.3 CAD design

As our structure is a very specific structure which combines grating couplers, waveguide and a resonator, we could draw manually the design taking into account the previously calculated parameters. However, for our different test in lithography, etching and characterization of the device, it is better for us to make a code for the CAD design. It is well known that there are softwares that allow the user to design Photonic devices adjusting the required the parameters, but considering that our design doesn't has a lot of photonic components, it is not required to use one of them. This is why we preferred to create a python code which allow us to change the dimensions of the general design shown in the figure 2.1. The inputs of the program are shown in the figure 4.6.

The screenshot shows a window titled "Optical Resonator Designer" with the following parameters and values:

Parameter	Value
Waveguide width (um)	2
Waveguide length (um)	200
Linewidth (um)	0.308
Coupler period (um)	0.616
Number of circle segments	163
Aperture angle (°)	40
Distance from waveguide edge to bragg coupler (um)	5
Add contour to the design (1 for yes, 0 for no)	0
Distance of separation of the contour (um)	0.308
Width of the contour (um)	0.2
Add DBR to the design (1 for yes, 0 for no)	0
DBR Cavity length (um)	5
DBR period (um)	0.616
DBR linewidth (um)	0.308
DBR number of lines	10

At the bottom of the window is a button labeled "Draw waveguide with grating coupler".

Figure 4.6: Python program for the design of the optical resonator (the values on the picture are example values). Code on appendix A

4.4.4 First test lithography

In the first test, we used the python code to design a short waveguide without resonator and connected to the two grating couplers. The design is shown at figure

4.7.

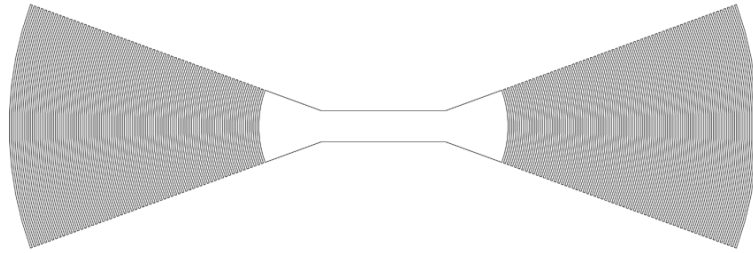


Figure 4.7: CAD design of a short waveguide test.

After doing the lithography, we realized that there were some impurities at the time of developing the sample. But the dimensions were quite the same as planned with the CAD. The results with a tilt of 70° are shown in the figure 4.8. What it is important to be sure is the high contrast ratio of the resist when exposed, as we do not want resist to be between structures, since the resist will be used as a mask for etching.

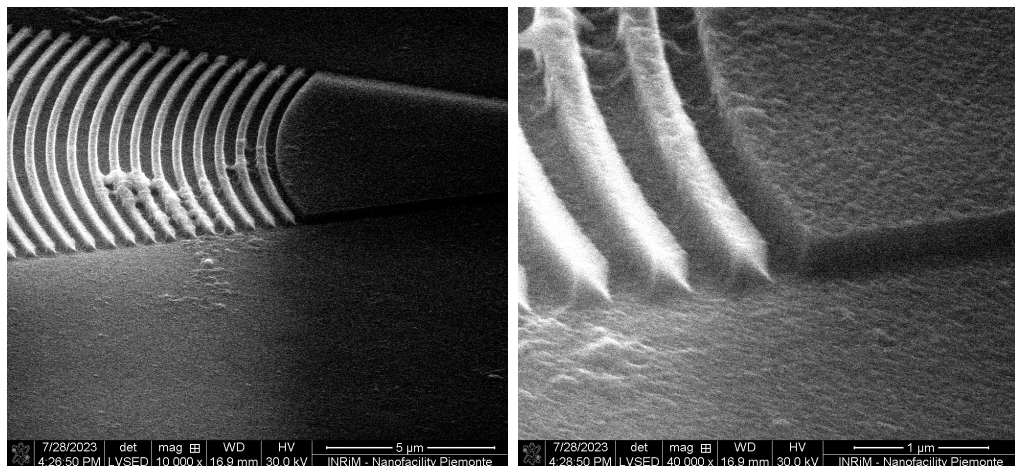


Figure 4.8: SEM images showing the result of the lithographic process of the grating coupler and waveguide together

4.4.5 Second test lithography

The second test lithography was made to characterize the waveguide at different lengths, but in this case the parameters of the number of lines (163), the distance from the waveguide edge to the grating coupler ($5\mu m$) and the waveguide width

($2\mu m$) are different from the previous one since we are approaching the final design. The purpose of these lithographies is to vary the waveguide length in order to calculate the losses inside the waveguide (figure 4.9). However, as we increase the size of the waveguide, it is necessary to reduce the magnification of the SEM in order to obtain a bigger field of view available to do the lithography; and one problem arises: if we decrease the magnification of the SEM, we're decreasing the resolution of the EBL, thus the writing of small features would not be the wanted one.



Figure 4.9: CAD design of a long waveguide. The coupling grating seem to be completely fill but is due to the sampling of the image as the grating lines are thin

To solve the previous problem, one solution was to separate the CADs to write the grating coupler and the waveguide separately, in this way we can change the magnifications when writing each design part. What we do is to move the sample the required distance to adjust the design to the original one. In this way, the first design is the left grating, the second design is the waveguide and the third design is the right grating. After writing the first design, the samples moves and the second design is written and the same happens with the third one.

However, there are some problems with this solution because the displacements of the SEM do not have the precision we require. When the sample moves, the displacement is controlled by some motors which have a micrometric precision, not a nanometric one. Thus the final lithography is a shifted and rotated one, something that can be seen in the figure 4.10.

One solution for the problem would be to combine optical and EBL lithographies. Since the waveguide has a thickness which is in the order of the microns, it is possible to do it with photolithography. So the process is separated in two implementations. It is important to consider the writing of markers when doing the photolithography process in order to use them in the alignment option available at EBL. This option allow us to align the waveguide with the grating couplers as they are separated. In addition, this process would be useful for the resonant cavity too as the the required resolution for the grating is high.

4.4.6 Combination with Photolithography

When combining both lithographies, the order of the procedures are important for the good fabrication of the device:

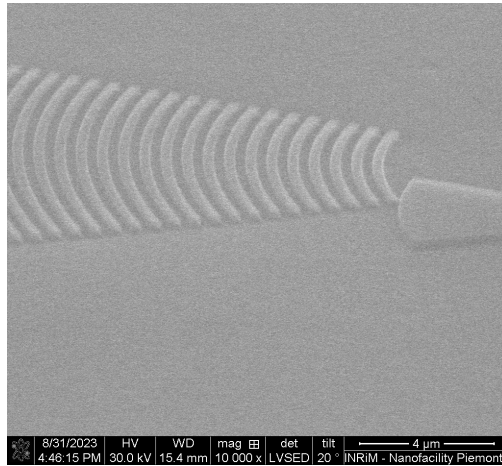


Figure 4.10: Result of the lithographic process with separated CAD designs. A displacement and a rotation can be seen between the grating coupler and the waveguide.

1. First, the photolithography process is done in a way to obtain the waveguide only (without the couplers) and alignment marks for the posterior alignment.
2. Second, a deposition of a metal (Aluminum in this case) is performed in order to do a lift off of the mask, thus it is crucial to do a positive photolithography process in the previous step. Metal is deposited in the sample for the purpose of increasing the contrast when doing EBL. This metal layer is also used as mask for the waveguide etching.
3. Finally, when doing the EBL process, we perform an alignment of the marks and the CAD with the help of NPGS, the alignment is done in order to rotate and shift the CAD in the field of view of the EBL, thus the sample is not moved. The procedure is done in a way the place where the lithography will be performed is not written when aligning.

The final lithography with the alignment is shown at figure 4.11.

4.4.7 Isolated Resonator lithography

Before proceeding with the whole device lithography, it is important to check the lithography of the resonator only to verify that a lithography with such dimensions is feasible. For this purpose we use the previously calculated parameters and design a CAD of the resonant cavity (fig 4.12) with the two Bragg mirrors and two short waveguides to see how will behave the structure after doing the exposure. The results of the EBL lithography are shown in the figure 4.13

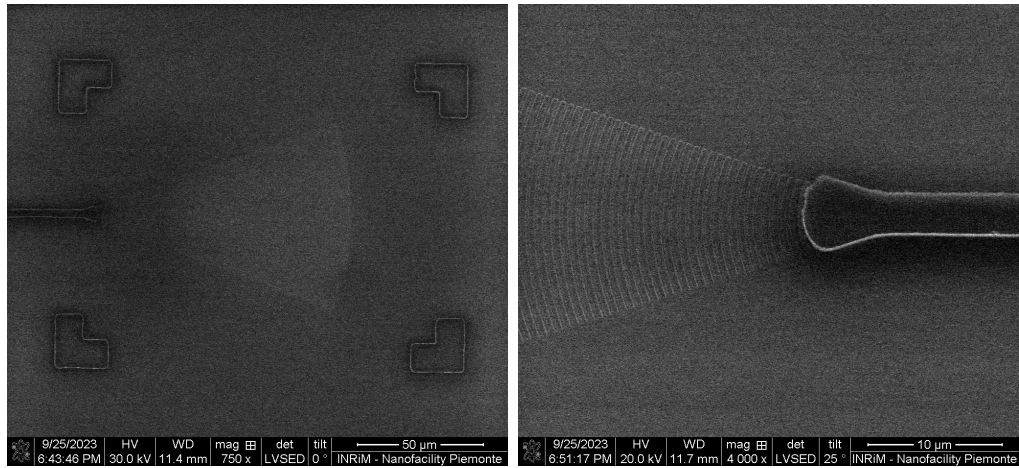


Figure 4.11: Result of the lithographic process with the alignment process combining optical lithography and EBL. At left, the waveguide and alignment marks mask can be seen with high contrast as these are made of aluminum, while at the center the grating coupler is made of resist. At right, it can be seen that the alignment was successful and good coupling of the grating with the waveguide could be achieved thanks to this process.

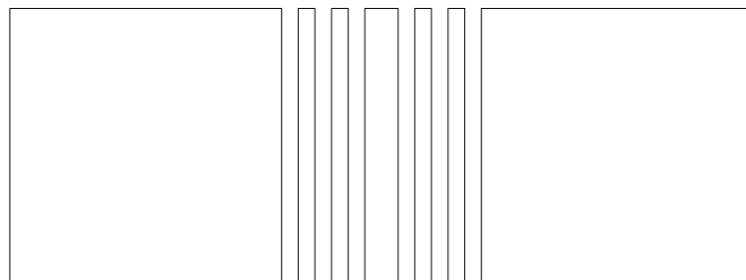


Figure 4.12: CAD of the resonator with two additional short waveguides

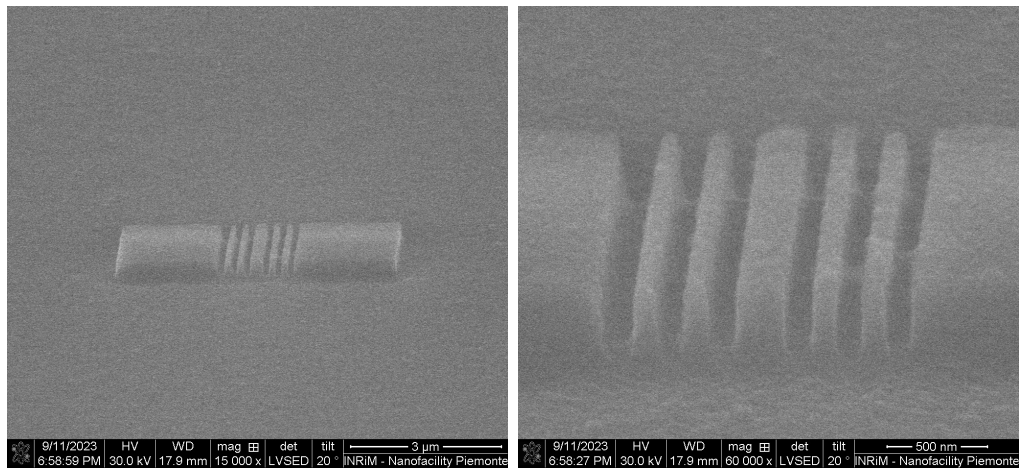


Figure 4.13: Result of EBL lithography of the resonator

Chapter 5

Etching

5.1 Reactive Ion Etching

5.1.1 Description

Reactive Ion Etching (RIE) is a form of dry etching. In dry etching, the etch reactants originate from a gas or vapor-phase source and are usually ionized. The reactive species that etch the exposed film are atoms or ions from the gas. There are two types of dry etching: plasma-based and non-plasma-based. [16]

For a RF plasma-based dry etching, the next steps are followed:

1. Chamber is evacuated
2. Chamber is filled with the etchant gases
3. RF energy is applied to a pair of electrodes
4. Applied energy accelerates electrons, thus increasing the kinetic energy.
5. Electrons collide with neutral gas molecules, forming ions and more electrons.
6. Steady state is reached (plasma), where ionization is equal to recombination.

This process is akin to PECVD, except that etch gas is employed instead of precursor gas. In this process, both chemical and physical etching take place. Moreover, etching is relatively isotropic and selective due to the potent chemical component.

RIE is similar to a sputter etcher, but instead of noble gases, we employ reactive gases similar to those used in plasma etching. The objective is to have high-energy ions at the surface, so we apply high accelerating voltages and low pressures. For both plasma etching and RIE, the feed-gas composition generates the reactive

species necessary for etching. The chemistry tends to be isotropic, and the ion bombardment of surfaces creates anisotropy in plasma-assisted pattern transfer.

By examining the relationship between pressure and ion energy, we can observe that lower pressure leads to an increase in the mean free path and voltage drop near the wafer electrode. This enables a more energetic and directional ion bombardment, thereby enhancing anisotropy. However, the etching rate decreases as the density of ions or free radicals diminishes.

1. Plasma mode: Pressure $> 100\text{mTorr}$
2. RIE mode: Pressure between 10mTorr and 100mTorr

The generator used for RIE is a ICP-RIE reactor, which has dual plasma source:

1. Top one (ICP) used to generate high-density plasma. This generator determines the ion density.
2. Bottom one (CCP RF) used to generate bias voltage. This generator determines the ion energy.

Lastly, the control parameters for etchant species generation are the following:

1. Gas selection
2. Flow rate and pumping speed, thus the pressure.
3. Applied power and frequency
4. Bias voltage on powered electrode

While the parameters regarding etchant interaction with the surface are:

1. Geometrical factors of the structure being etched
2. Temperature of the substrate (usually substrate is cooled)
3. Nature of the substrate (composition of the substrate)

5.1.2 Endpoint detector

The Endpoint detector is employed during wafer etching to ensure that the etch process stops at the ideal depth. By providing real-time feedback and control, the endpoint detector enables precise detection of when to stop. While there are two primary techniques for endpoint measurement, we utilize the Laser Interferometry technique. [30]

The laser interferometry technique monitors the wafer by directing a small laser spot onto its surface and gauging the intensity of the reflected light. A special

camera is positioned at the apex of the etch chamber, capturing an image of the wafer surface and focusing a laser spot onto it. This camera also captures the light reflected from the laser, which is used to determine the wafer's reflectance. The key advantage of this technique is its ability to measure small samples and etch depths within a transparent layer.

When the laser is focused on a single small spot, the endpoint trace will exhibit layer interfaces with great clarity, particularly under high contrast conditions. In the case of etching a transparent layer, the etch depth can be determined by counting ripples in the reflected intensity. These ripples arise from interference effects within the layer as its thickness varies. If we are etching until depth via ripple counting, the accuracy is generally $\pm 1\%$ or less; this assuming a sufficient number of ripples in the reflectance and that the refractive index of the etched layer is well characterised.

5.1.3 Etching of SiN

A recipe for SiN was used, but the results were not good as the etching was too slow or even not present. The recipe for SiN nitride etching was doing more physical etching than a chemical one. Because of this, the recipe was changed considering that the material was not an stoichiometrical one, since the concentration of Si was higher than the concentration of N given by the XPS data. Thus the recipe was changed to a Silicon-etching recipe, in which the Pseudo Bosch process is used to obtain a high aspect ratio of the structures.

The Bosch Process is a high-aspect ratio plasma etching process. The process consist of the cyclic isotropic etching and fluorocarbon-based protection film deposition by quick has switching. The SF₆ plasma cycle etches silicon, and the C₄F₈ plasma cycle creates a protection layer. To achieve deep silicon etching with high aspect ratio, both of the SF₆ plasma cycle and C₄F₈ plasma cycle need to be optimized. The protection film needs to be thick enough to withstand the SF₆ plasma cycle for highly anisotropic silicon etching. [31]

In this case we used a non-cyclic process: the Pseudo-Bosch process in which the gases enter the chamber simultaneously, therefore the protection film and the etching is done also simultaneously and the gases ratio should be well configured. By etching a clean sample with SiN, it could be possible the fading of the yellowish layer above the substrate, thus the etching has was well chosen. The parameter for this recipe are:

1. RF power: 30W
2. ICP power: 1200W
3. Si₄F₆ gas flow rate: 50 sccm

4. C_4F_8 gas flow rate: 50 sccm

Then a sample with a previous lithography above in which we made the lift-off process to have a Aluminum mask is used for the etching test: the results show that the recipe could work for long etching times (figure 5.1). After the etching, the hard mask of aluminum was removed to see the real profile of the structures: the results show that the recipe could be a good option.

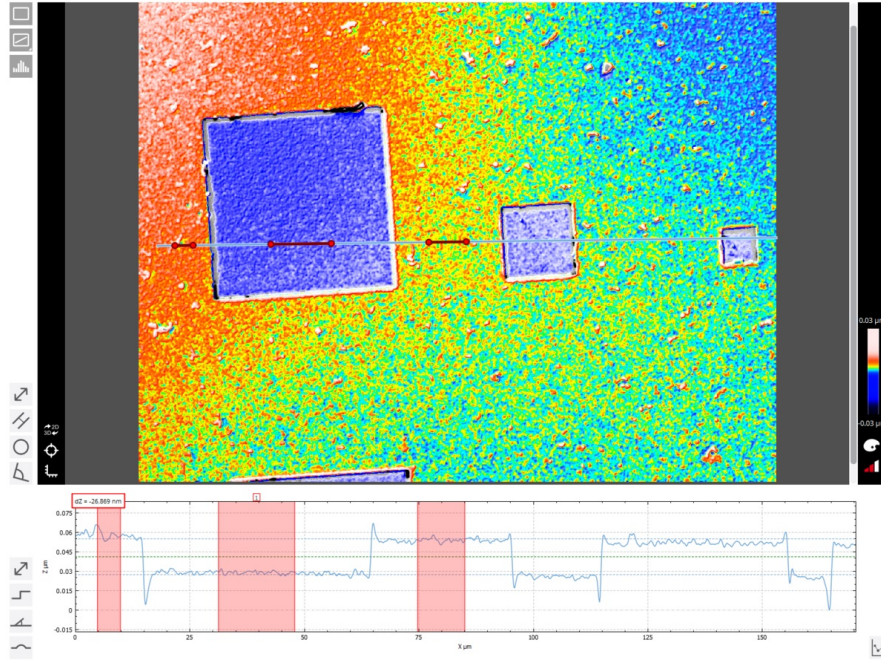


Figure 5.1: RIE test for the circles and squares lithography. Data taken with optical profilometer

We tried to etch an EBL lithography with the same etching parameters and only using resist as a mask (ma-n2401). The results shown that maybe the resist was not thick enough to be used as a mask for the etching process (figure 5.2). We tried to increase the selectivity by using an Aluminum mask with a previous lithography using a positive resist (PMMA), however, we had another problem here since the grating lines linewidth was reduced and the mask was no longer above the material (figure 5.3).

At the end we end up using the EBL resist ma-n2405 to increase the resolution and the thickness of the etching mask. With this solution we increased the thickness of the final structures, nevertheless the mask was not still present when the etching arrived till the end of the material layer as shown in the figure 5.4. This is an unwanted feature as we want the waveguide to be as flat as possible to avoid scattering of light.

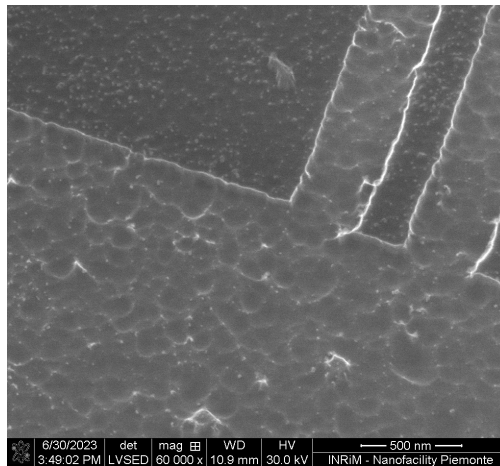


Figure 5.2: RIE test for EBL lithography using resist ma-n2401 as a mask

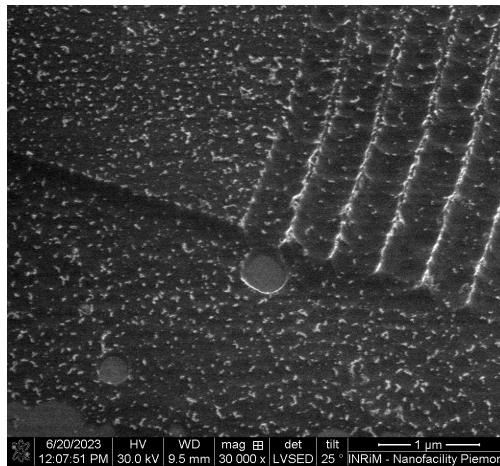


Figure 5.3: RIE test for EBL lithography using resist Aluminum as a mask

With all of these results in mind, we stop trying changing the mask but the etching parameters to increase the selectivity of SiN over the resist. Considering the paper written by M. D. Henry et al [32] the authors use a Pseudo-Bosch process with the same gases used by us. However, the gas flow rates ratio are different and the acceleration RF power also differs. Thus the new etching parameters are:

1. RF power: 20W
2. ICP power: 1200W
3. Si_4F_6 gas flow rate: 33 sccm
4. C_4F_8 gas flow rate: 57 sccm

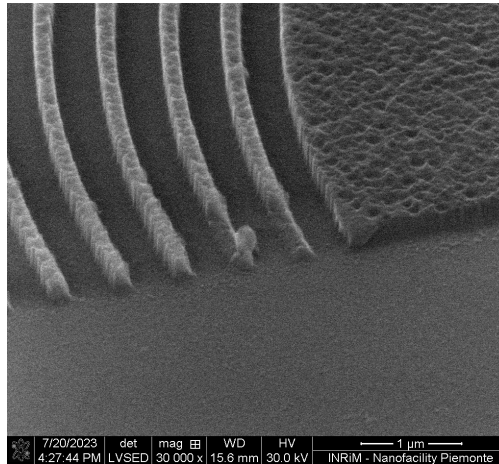


Figure 5.4: RIE test for EBL lithography using resist ma-n2405 as a mask

With this recipe, the density of ion or free radicals is kept the same, but as we are reducing the RF power, the energy of the ions is reduced, thus the physical etching is reduced with respect to the chemical one. Another important parameter is the gases flow rate ratio: the C_4F_8 concentration is increased to stay higher than the Si_4F_6 concentration. In this way the C_4F_8 gas has enough time to create the passivation film for the sides, therefore the linewidth of the grating lines is kept almost constant. The result can be seen in the figure 5.5, where the resist still remains as a mask, something we want to keep the flatness of the SiN layer. This etching was done in a sample with SiN with thickness of around 550nm, thus the final device thickness should not be the one shown in the figure but less (200nm), but as this is a test for the etching recipe it is even better because a high aspect ratio is in evidence.

5.1.4 Etching rate

By using the endpoint detector, it is possible to measure the etching rate of SiN with the last used etching recipe. From all the samples we have deposited we only achieved a good etching for the last ones. In the figure 5.6, it is shown that there are ripples due to the laser interferometry since a layer of SiN is being etched. However, a period change between the first interval (0s to 190s) and the second (190s to 348) is present, this could mean that what we are etching is not a single material layer but two. One hypothesis for this is that what we are etching at the beginning is a thin layer of resist that still remained above the substrate after the development, then the second interval is what we really care about. Once the ripples disappeared or change in an abrupt way, it means that we're meeting another layer (in this case Glass). As the recipe is thought to have a high selectivity to SiN, the glass acts

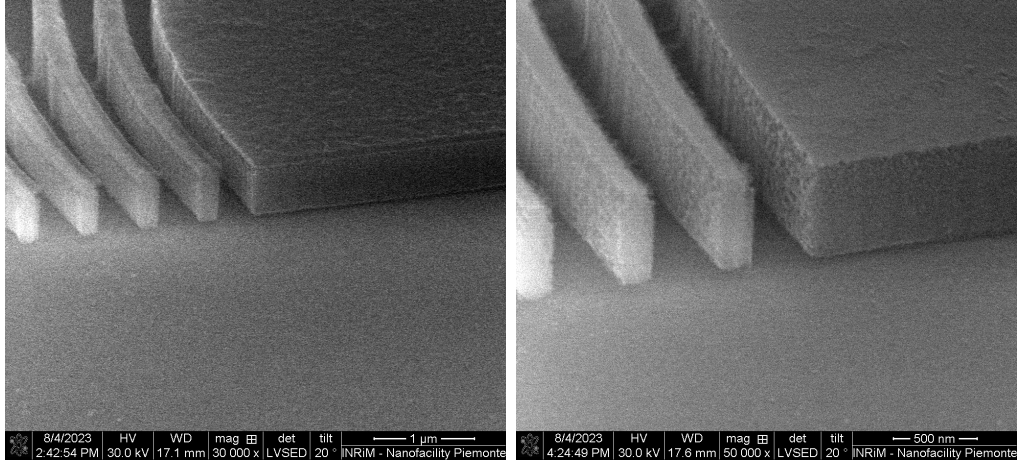


Figure 5.5: RIE test for EBL lithography using resist ma-n2405 as a mask. At the left image the structure still have the resist mask above. At the right the resist mask is removed

as a etching stop layer. In this way the way to know that we reach the bottom is checking for a zero derivative reflectance signal.

Assuming that the etching of SiN is linear and it starts when the second interval begins, the etch depth for a single period is:

$$d_{period} = \frac{\lambda_{laser}}{2n_{SiN}}$$

Where λ_{laser} is the wavelength of the laser used for interferometry (670nm in this case [33]) and n_{SiN} is the refractive index of the SiN layer. This means that for 4 periods seen in the figure, we are etching around 582nm of SiN, something that makes sense as the sample had a nominal layer thickness of 570nm. To estimate the etching rate from the acquired data, we simply divided the thickness of the layer by the time of the second interval:

$$r_{etch} = \frac{570nm}{348.55s - 188.99s} \approx 3.57 \frac{nm}{s}$$

5.1.5 Final structures and problems

In the end, after the lithography processes, a final structure was obtained for each lithography. At figure 5.7 an optical resonator was created to test the effectiveness of the etching process at such small dimensions.

However, the final structure for the grating coupler and the waveguide is still in progress since the etching is not as good as we expected when doing the alignment.

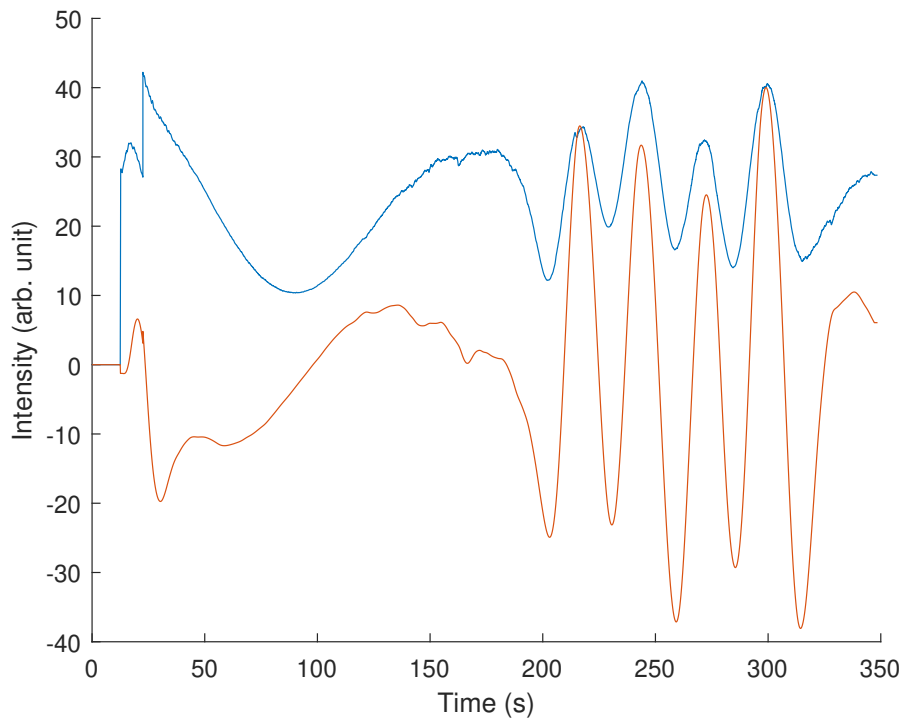


Figure 5.6: Reflectance intensity data when etching a sample with a layer of SiN

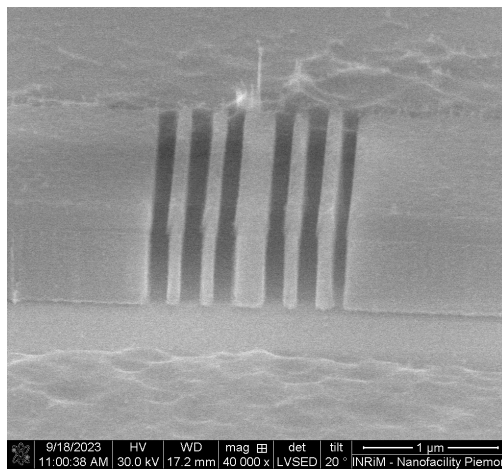


Figure 5.7: RIE test for EBL lithography of optical resonator

It can be seen in the figure 5.8 that the etching was better outside the structure, but between the grating lines it can still be improved, for the contrast of the EBL lithography wasn't the best. In addition, there was an accumulation of resist next to the coupling of the waveguide and the grating coupler that did not allow the

correct structure etching. The process for the alignment still needs optimization but is not done in this thesis due to the lack of time. One hypothesis for the cause of low contrast in the lithographic process is that the resist is accumulated between the alignment marks, thus increasing the thickness of the resist and therefore increasing the required exposure dose.

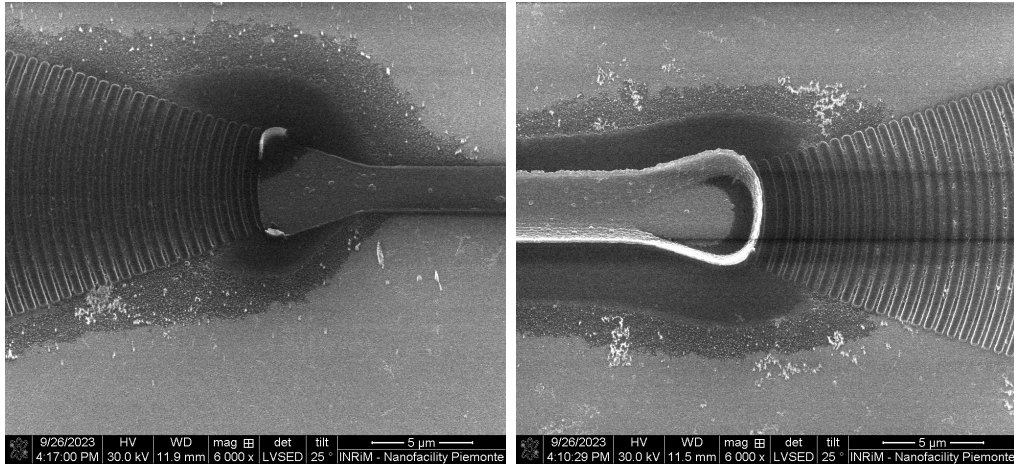


Figure 5.8: RIE of grating coupler aligned with waveguide

To test the coupling efficiency of the gratings, a structure was made without the alignment, thus with only one lithographic step. In the figure 5.9 the mismatch discussed previously is present, however it seems that the grating is at the right angle with the waveguide and could be enough for the light coupling. This sample was made with a grating period designed to couple light at normal incidence, as explained in the next chapter.

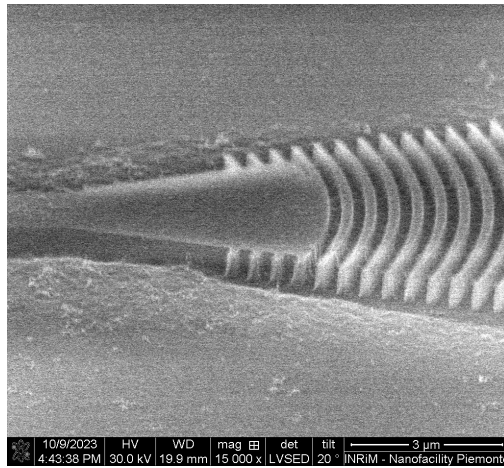


Figure 5.9: RIE of grating coupler aligned with waveguide

Chapter 6

Device characterization

Once we have the final structure, the waveguide and the resonator can be characterized. The waveguide can be characterized by implementing a lithography with different lengths: this is done in order to calculate the extinction coefficient when the wave travels inside the material. Considering that when light passes through a medium, part of the light will always be absorbed, thus the complex refractive index is defined as [34]:

$$\underline{n} = n + j\kappa$$

A wave travelling in x direction has an electric field in the form:

$$E(x, t) = E_0 \exp(j(\underline{k}x - \omega t)) = \exp(-2\pi\kappa x/\lambda_0) E_0 \exp(j(kx - \omega t))$$

This means that the inclusion of the extinction coefficient (κ) in the complex refractive index results in an exponential decay depending on the traveled distance. By increasing the distance, the field intensity is reduced, and by varying the waveguide length, there will be enough information for the extinction coefficient calculation (or absorption coefficient).

The measurement is done by applying an excitation light at one grating coupler and the output is measured at the grating coupler on the other side of the waveguide as shown in the figure 6.1 (The probes should have an inclination angle for the coupling of the light with the waveguide). Of course this measurements will include some losses given by the grating couplers. In order to apply this excitation, a probe station is needed, where the injection of light from an optical fiber can be optimized.

On the other hand, for the characterization of the resonator, the lithography should include the two Bragg mirrors and the cavity. The difference is that in here we only measure the light spectrum (frequency response) at the output for a given input. What we expect should be something shown at the figure 2.15.

In this work, no characterization was performed since the device will be characterized in the laboratories of another research institute and there was no source of

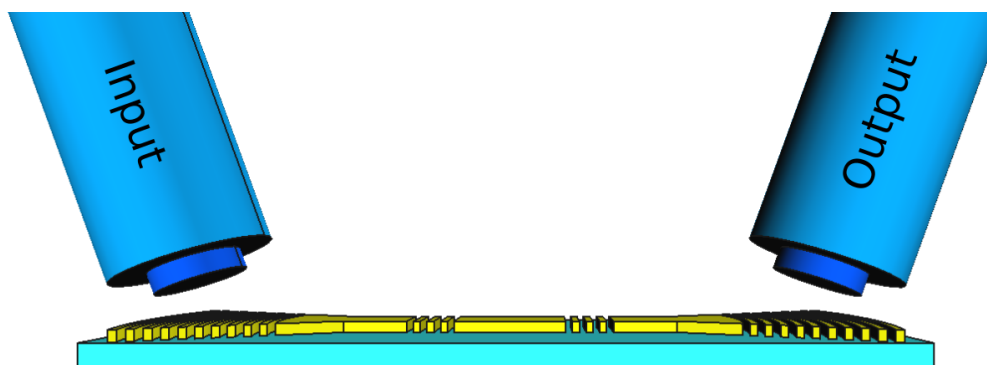


Figure 6.1: 3D model side view of the device and the 2 optic fibers for the input and output signal

light for the spectrum response of the device. Therefore, only simple tests of the waveguide without the resonator were made at our institute for now.

6.1 Waveguide and grating response

In order to test the coupling efficiency of the gratings on our setups we fabricated a grating coupler with a different period (a period that will allow us to couple at 0°) for perpendicular coupling. A laser with the required wavelength was focused by an optical condensator onto the grating, then an image is obtained with light collected from the bottom as shown in the figure 6.2

The result for this setup is shown in the figure 6.3. Where it can be seen that when focusing the laser beam into the grating coupler, there is no emitted light at the other side. This could mean that most of the high intensity modes are not being transport into the waveguide or that the coupling is not successful. This is verified when seeing 2 spots at the two sides of the sample (fig 6.4), meaning that the grating works but the light is not being coupled into the waveguide, instead is transferred into the glass substrate. When the laser beam is being put just above the grating, the sample starts to glow as if the substrate were acting as a waveguide (fig 6.5).

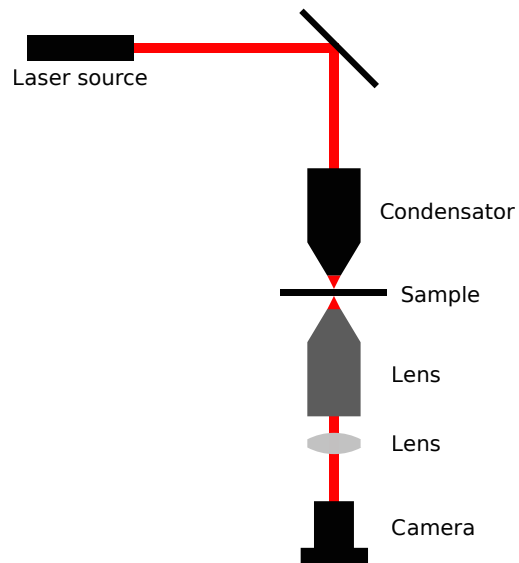


Figure 6.2: Simplified setup for the waveguide test

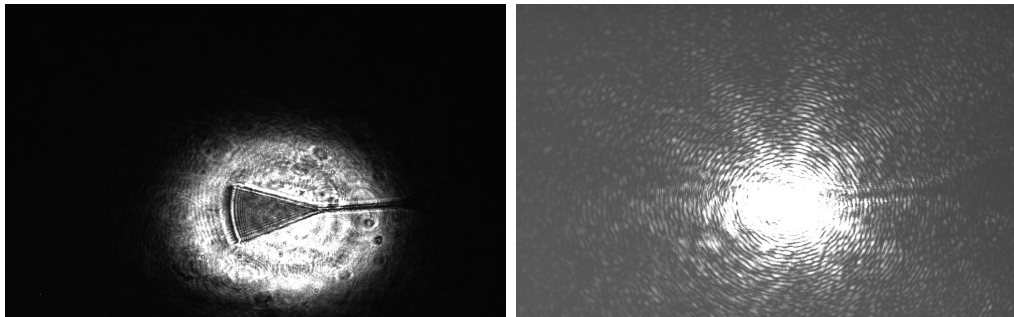


Figure 6.3: Waveguide test for perpendicular coupling. At the left image the spot of the input laser beam is big enough to illuminate a great part of the grating. At the right image, the spot is reduced and the image exposure time is increased in order to see the entire waveguide, but no emitted light is seen at the output

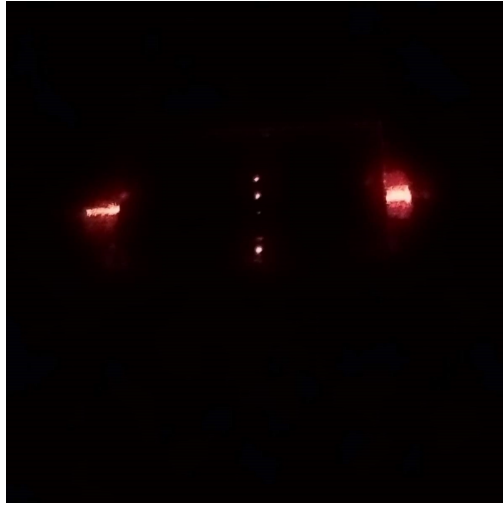


Figure 6.4: Sample being illuminated with the laser spot above the grating. The waveguide is horizontal, thus there are two laser spots at left and right side of the sample



Figure 6.5: Illuminated sample with condensator. At the left image, the sample is being illuminated with a focusing beam outside the grating coupler. At the right image, the laser spot is inside the grating, the sample glows due to the light confinement inside the substrate since the glass substrate is acting as a waveguide.

Chapter 7

Alternative strategies to confine light

One option for the confinement of light is to use a metasurface as a mirror instead of a Bragg mirror. Metasurfaces are composed of numerous nanoresonators called meta-atoms. The arrangement of these meta-atoms affects light scattering, leading to local modulation of the amplitude and phase of the electric and magnetic fields. By selecting the geometrical dimensions, orientation, and material of each nanoresonator, it is possible to achieve a high degree of freedom for engineered light scattering. [35]

The article describes how transmission and reflection are modulated using an infinite array of high refractive index nanopillars arranged in a square lattice configuration. The unit cell consists of a glass substrate with a pillar standing on it, and periodic boundary conditions are applied to the unit cell. The results indicate that varying the height of the nanopillars shifts the resonance frequency and increases the Q-factor up to 10^5 at specific frequencies (fig 7.1). This is noteworthy because the high Q factor could be used for laser applications where a narrow linewidth is important. Additionally, varying the pitch (P) of the unit cell also shifts the transmittance.

One idea for the implementation of a resonator with this metasurface is patterning the cylinder array in the substrate of the sample, then an optical fiber is used as the second mirror: in this way the cavity is located between the metasurface and the optic fiber. In this configuration the optic fiber is already coupled to the system so there is no need for a coupler like the grating coupler. A diagram of the resonator can be seen in the figure 7.2

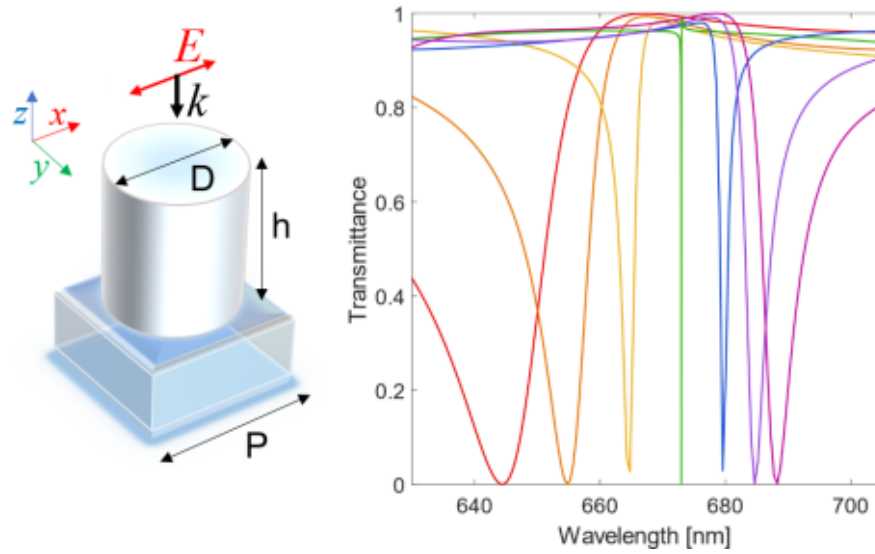


Figure 7.1: At the left, the unit cell consisting of a diamond nanopillar on a glass substrate with the indicated dimensions: D is the diameter of the cylinder, h is the height of the cylinder and P is the pitch. At the right the Transmittance response is shown at different cylinder heights

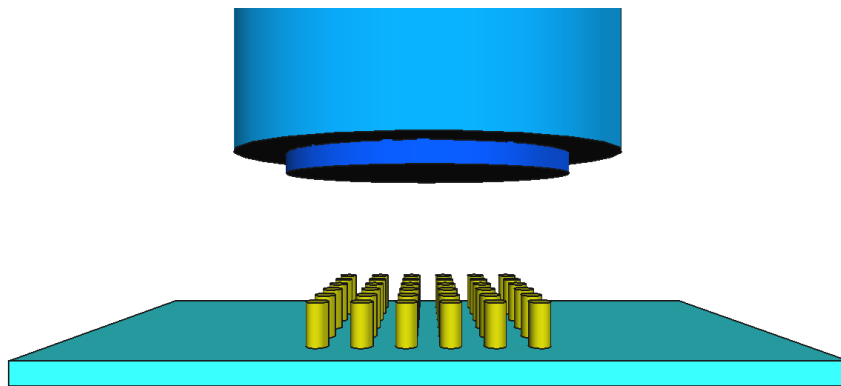


Figure 7.2: Idea for a resonator composed by a metasurface (at the bottom) and an optical fiber (at the top), where the fiber acts as a mirror at the interface

7.1 Working principle of the metasurface

Rayleigh scattering is the process of light or other electromagnetic radiation being scattered by particles that are much smaller than the wavelength of the radiation. This type of scattering is mostly elastic. When the frequency of the light is lower

than the resonance frequency of the scattering particle, the amount of scattering is inversely proportional to the fourth power of the wavelength. [36]

The scattering occurs due to the electric polarizability of the particles. When a light wave's oscillating electric field interacts with the charges of the particle, it causes them to move at the same frequency. Consequently, the particle behaves like a small radiating dipole, leading to the scattering of light (fig 7.3).

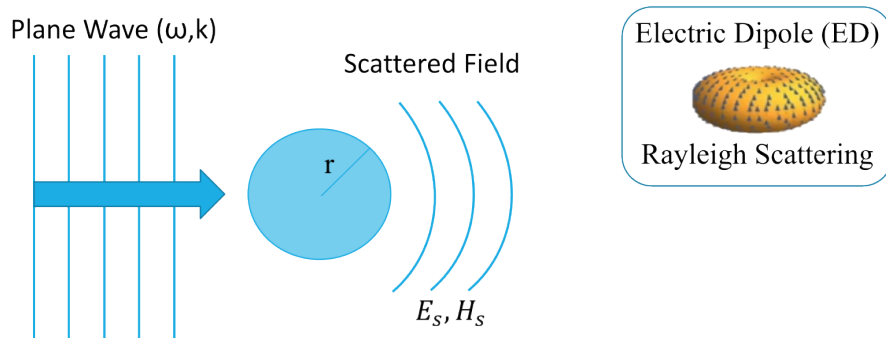


Figure 7.3: Rayleigh scattering description

When the size of the particles is comparable to or larger than the wavelength of light, Mie theory is used to describe the scattering. Mie scattering is the solution to Maxwell's equations that describes the scattering of an electromagnetic plane wave by a homogeneous sphere. The solution takes the form of an infinite series of spherical multipole partial waves (fig 7.4) [37]. In this way, the final scattered field is the sum of an electric dipole, a magnetic dipole, an electric quadrupole, and so on.

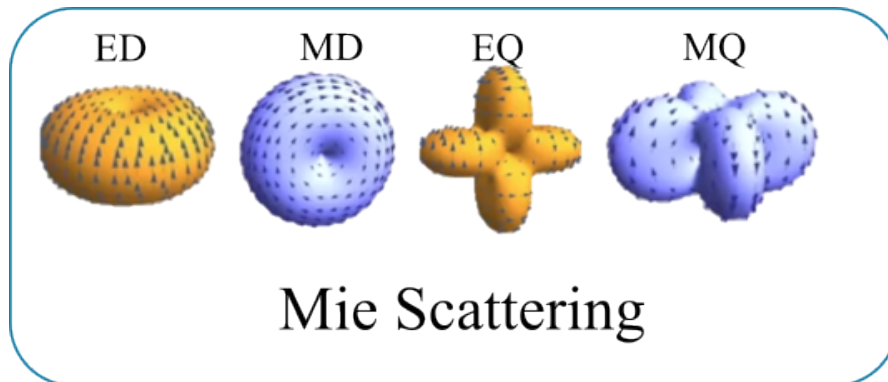


Figure 7.4: Mie scattering generated poles: Electric dipole, Magnetic dipole, Electric quadrupole, Magnetic quadrupole, etc

The coefficients of the series for the final forward and backward scattered wave

are:

$$C_s^{forward} = \frac{1}{a^2 k^2} \left| \sum_{n=1}^{\infty} (2n+1)(a_n + b_n) \right|^2$$

$$C_s^{backward} = \frac{1}{a^2 k^2} \left| \sum_{n=1}^{\infty} (2n+1)(-1)^n (a_n - b_n) \right|^2$$

In the article written by Kerker et. al [38], the authors explain that when the magnetic permeability and the dielectric permittivity are equal ($\mu = \epsilon$), so are the coefficients a and b ($a_n = b_n$). This means that the the final backward scattering is zero and the only type of scattering is the forward one. This is the main behavior behind the suggested metasurface.

7.2 Electric and magnetic poles in the metasurface

When varying the height of the cylinder, there is a point where the Q factor is maximized. At this point, two magnetic dipoles and one electric quadrupole are created inside the cylinder (fig 7.5), allowing the scattering for the previously shown transmittance response.

7.3 Metasurface implementation

To test if the structure implementation is feasible, a whole process of lithography and etching was made. First a CAD consisting of an array of filled circles was created, then we followed the same EBL lithography process as the one previously done for the grating coupler. Finally an etching step was done to obtain the pillars as shown in the figure 7.6. The CAD occupies an area of $64\mu m \times 64\mu m$, consisting of circles of diameter $D = 220nm$, height the same as the SiN layer ($H \approx 550nm$) and pitch of $P = 330nm$, in this way 200 circles by each side can fit the area.

By illuminating the metasurface with collimated white light, the transmitted light can be collected and the spectrum analyzed with a spectrometer. In this way, the frequency response can be measured since the white light contains a broad spectrum. After collecting the data, by doing a comparison between the simulated and experimental data (figure 7.7), it can be seen that the simulated spectra both show three resonances, although there is a shift probably due to geometrical differences. In this case the simulation was performed taking into account the real parameters of the metasurface, this is the real dimensions of height, diameter and period taken from the SEM microscope; this is why there are three resonances instead of one as shown before.

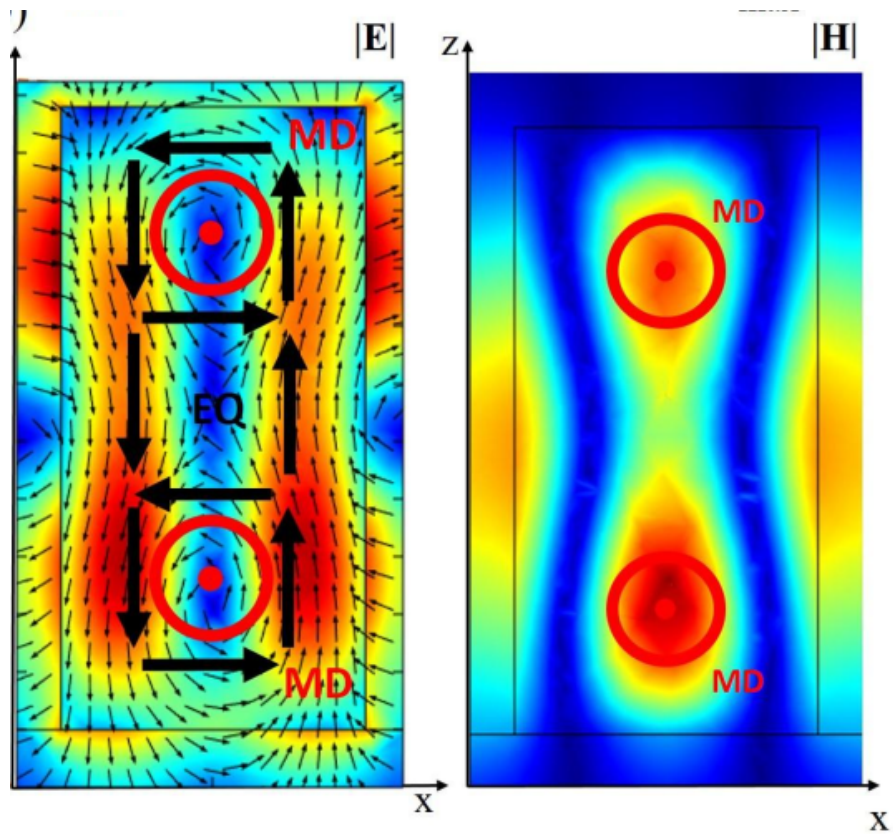


Figure 7.5: Lateral view of the cylinder electric (E) and magnetic (H) fields. The flux lines show the creation of two magnetic dipoles and one magnetic quadrupole

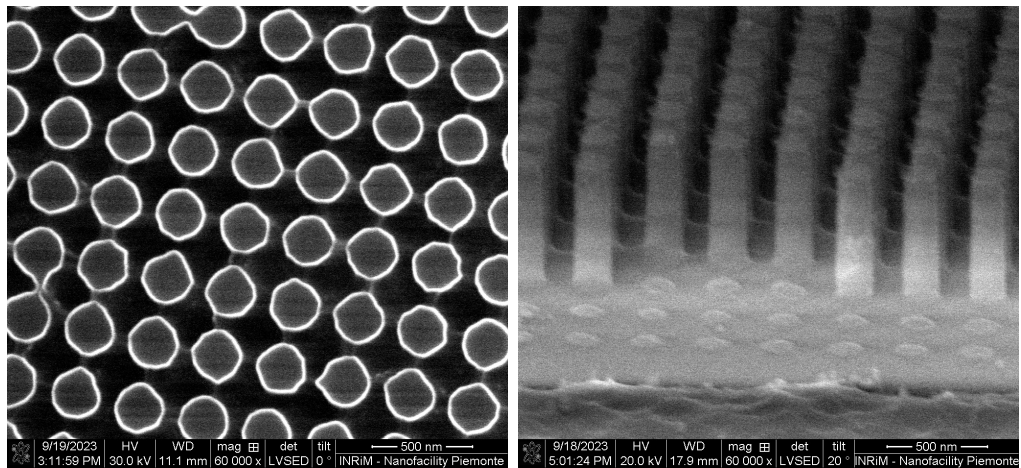


Figure 7.6: SEM image of the sample after doing RIE process on it. An EBL patterning of a circle matrix was done before to use the resist as a mask for etching

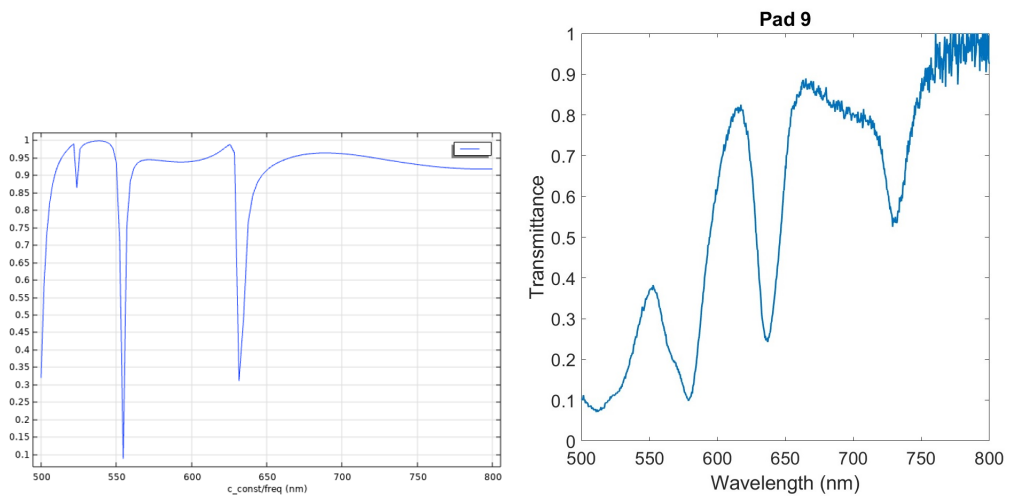


Figure 7.7: Comparison of simulated and experimental results. At the left image, the simulated optical transmittance with COMSOL. At the right image, the experimental optical transmittance of the metasurface. There are 3 resonance frequencies where the reflection is increased

Appendix A

Code implementation for CAD design

```
1 import ezdxf
2 import math
3 import numpy as np
4 import tkinter as tk
5
6 # Convert from cartesian to polar
7 def cart2pol(x, y):
8     rho = np.sqrt(x**2 + y**2)
9     phi = np.arctan2(y, x)
10    return(rho, phi)
11
12 # Convert from polar to cartesian
13 def pol2cart(rho, phi):
14     x = rho * np.cos(phi)
15     y = rho * np.sin(phi)
16    return(x, y)
17
18 # Sum of cartesian coordinates:
19 def sum_of_cart_coord(a, b):
20     coord = [(a[i] + b[i]) for i in range(len(a))]
21    return tuple(coord)
22
23 def neg_of_cart_coord(a):
24     coord = [(-a[i]) for i in range(len(a))]
25    return tuple(coord)
26
27
28
```

```

29 def draw_waveguide_coupler():
30     # create a new DXF R2010 document
31     doc = ezdxf.new("R2010", setup=True)
32     doc.set_modelspace_vport(height=10, center=(0, 0))
33
34     # add new entities to the modelspace
35     msp = doc.modelspace()
36
37     # Define the units of the file
38     doc.header["$INSUNITS"] = 13 # 13 for microns
39
40     # Variables:
41     waveguide_width = float(fields['waveguide_width'].get())
42     waveguide_lenght = float(fields['waveguide_lenght'].get())
43     linewidth = float(fields['linewidth'].get())
44     distance_between_circles = float(fields['distance_between_circles
45     '].get())
46     aperture_angle = float(fields['aperture_angle'].get())
47     number_of_circles = int(fields['number_of_circles'].get())
48     d_waveguide_coupler = float(fields['d_waveguide_coupler'].get())
49     add_contour = int(fields['add_contour'].get())
50     separation_contour = float(fields['separation_contour'].get())
51     width_contour = float(fields['width_contour'].get())
52
53     add_dbr = int(fields['add_dbr'].get())
54     dbr_cavity_lenght = float(fields['dbr_cavity_lenght'].get())
55     dbr_period = float(fields['dbr_period'].get())
56     dbr_linewidth = float(fields['dbr_linewidth'].get())
57     dbr_number_lines = int(fields['dbr_number_lines'].get())
58
59     ## Calc of angles to rad (index 0 for right, 1 for left)
60     start_angle_rad = (-(aperture_angle/2)/180*math.pi, (-(
61     aperture_angle/2)+180)/180*math.pi)
62     final_angle_rad = ((aperture_angle/2)/180*math.pi, ((
63     aperture_angle/2)+180)/180*math.pi)
64     aperture_angle_rad = aperture_angle/180*math.pi
65
66     start_angle_DBR_rad = (-(aperture_angle/2)/180*math.pi, ((
67     aperture_angle/2)+180)/180*math.pi)
68     final_angle_DBR_rad = ((aperture_angle/2)/180*math.pi, (-(
69     aperture_angle/2)+180)/180*math.pi)
70
71     # Calcs before the design
72     coupler_first_radius = waveguide_width/(2*np.sin(
73     aperture_angle_rad/2))
74     coupler_shift = math.sqrt(coupler_first_radius**2-waveguide_width
75     **2/4)

```

```

70 coupler_center_absolute = ((waveguide_lenght/2-coupler_shift, 0),
71                             -(waveguide_lenght/2-coupler_shift), 0)
72
73 # Design of the waveguide
74 if add_dbr == 1:
75     # Design of the cavity
76     points_cavity = []
77
78     pos_0 = (-dbr_cavity_lenght/2, -waveguide_width/2)
79     points_cavity.append((pos_0[0], pos_0[1], 0, 0, 0))
80
81     pos_1 = (dbr_cavity_lenght/2, -waveguide_width/2)
82     points_cavity.append((pos_1[0], pos_1[1], 0, 0, 0))
83
84     pos_2 = (dbr_cavity_lenght/2, waveguide_width/2)
85     points_cavity.append((pos_2[0], pos_2[1], 0, 0, 0))
86
87     pos_3 = (-dbr_cavity_lenght/2, waveguide_width/2)
88     points_cavity.append((pos_3[0], pos_3[1], 0, 0, 0))
89
90     pos_4 = pos_0
91     points_cavity.append((pos_4[0], pos_4[1], 0, 0, 0))
92
93     msp.add_lwpolyline(points_cavity)
94
95     first_distance = dbr_cavity_lenght/2 - dbr_linewidth/2 +
96     dbr_period
97     line_vector = [(first_distance + dbr_period*i) for i in range
98     (dbr_number_lines)]
99     bragg_constants = (1,-1)
100    for bragg_mirror in range(2):
101        for line in line_vector:
102            dbr_drawing = []
103            line_pos = (line+dbr_linewidth/2)*bragg_constants [
104            bragg_mirror]
105            line_neg = (line-dbr_linewidth/2)*bragg_constants [
106            bragg_mirror]
107
108            pos_0 = (line_neg, -waveguide_width/2)
109            dbr_drawing.append((pos_0[0], pos_0[1], 0, 0, 0))
110
111            pos_1 = (line_pos, -waveguide_width/2)
112            dbr_drawing.append((pos_1[0], pos_1[1], 0, 0, 0))
113
114            pos_2 = (line_pos, waveguide_width/2)
115            dbr_drawing.append((pos_2[0], pos_2[1], 0, 0, 0))
116
117            pos_3 = (line_neg, waveguide_width/2)

```

```

114         dbr_drawing.append((pos_3[0], pos_3[1], 0, 0, 0))
115
116         pos_4 = pos_0
117         dbr_drawing.append((pos_4[0], pos_4[1], 0, 0, 0))
118
119         msp.add_lwpolyline(dbr_drawing)
120
121         # Design of the waveguide after the cavity
122         initial_pos_dbr = line_vector[-1] + dbr_period -
dbr_linewidth/2
123         waveguide_constants = (1,-1)
124         for waveguide_side in range(2):
125             points_waveguide = []
126             if d_waveguide_coupler < (coupler_first_radius-
coupler_shift):
127                 R = coupler_first_radius
128                 # Point at the left down corner:
129                 pos_0 = (initial_pos_dbr*waveguide_constants[
waveguide_side], -waveguide_width/2)
130                 points_waveguide.append((pos_0[0], pos_0[1], 0, 0, 0)
)
131                 # Point at the right down corner:
132                 pos_1 = (waveguide_lenght/2*waveguide_constants[
waveguide_side], -waveguide_width/2)
133                 arc_left_right = ezdxf.math.arc_to_bulge((0,0),
start_angle_rad[waveguide_side], final_angle_rad[waveguide_side],
R)
134                 points_waveguide.append((pos_1[0], pos_1[1], 0, 0,
arc_left_right[2]*waveguide_constants[waveguide_side]))
135                 # Point at the right up corner:
136                 pos_2 = (waveguide_lenght/2*waveguide_constants[
waveguide_side], waveguide_width/2)
137                 points_waveguide.append((pos_2[0], pos_2[1], 0, 0, 0)
)
138                 # Point at the left up corner
139                 pos_3 = (initial_pos_dbr*waveguide_constants[
waveguide_side], waveguide_width/2)
140                 points_waveguide.append((pos_3[0], pos_3[1], 0, 0, 0)
)
141                 # Point at the left down corner:
142                 pos_4 = pos_0
143                 points_waveguide.append((pos_4[0], pos_4[1], 0, 0, 0)
)
144             else:
145                 R = d_waveguide_coupler + coupler_shift
146                 # Point at the left down corner:
147                 pos_0 = (initial_pos_dbr*waveguide_constants[
waveguide_side], -waveguide_width/2)

```

```

148         points_waveguide.append((pos_0[0], pos_0[1], 0, 0, 0)
149     )
150     # Point at the right down corner:
151     pos_1 = (waveguide_length/2*waveguide_constants[
152     waveguide_side], -waveguide_width/2)
153     points_waveguide.append((pos_1[0], pos_1[1], 0, 0, 0)
154     )
155     # Point at the right down extra corner:
156     pos_2 = sum_of_cart_coord(coupler_center_absolute[
157     waveguide_side], pol2cart(R, start_angle_DBR_rad[waveguide_side]))
158     arc_right = ezdxmath.arc_to_bulge((0,0),
159     start_angle_rad[waveguide_side], final_angle_rad[waveguide_side],
160     R)
161     points_waveguide.append((pos_2[0], pos_2[1], 0, 0,
162     arc_right[2]*waveguide_constants[waveguide_side]))
163     # Point at the right up extra corner:
164     pos_3 = sum_of_cart_coord(coupler_center_absolute[
165     waveguide_side], pol2cart(R, final_angle_DBR_rad[waveguide_side]))
166     points_waveguide.append((pos_3[0], pos_3[1], 0, 0, 0)
167     )
168     # Point at the right up corner:
169     pos_4 = (waveguide_length/2*waveguide_constants[
170     waveguide_side], waveguide_width/2)
171     points_waveguide.append((pos_4[0], pos_4[1], 0, 0, 0)
172     )
173     # Point at the left up corner
174     pos_5 = (initial_pos_dbr*waveguide_constants[
175     waveguide_side], waveguide_width/2)
176     points_waveguide.append((pos_5[0], pos_5[1], 0, 0, 0)
177     )
178     # Point at the left down corner:
179     pos_6 = pos_0
180     points_waveguide.append((pos_6[0], pos_6[1], 0, 0, 0)
181     )
182
183     msp.add_lwpolyline(points_waveguide)
184
185     else:
186         points_waveguide = []
187         if d_waveguide_coupler < (coupler_first_radius-coupler_shift)
188         :
189             R = coupler_first_radius
190             # Point at the left down corner:
191             pos_0 = (-waveguide_length/2, -waveguide_width/2)
192             points_waveguide.append((pos_0[0], pos_0[1], 0, 0, 0))
193             # Point at the right down corner:
194             pos_1 = (waveguide_length/2, -waveguide_width/2)
195             arc_right = ezdxmath.arc_to_bulge((0,0),
196             start_angle_rad[0], final_angle_rad[0], R)

```

```

181         points_waveguide.append((pos_1[0], pos_1[1], 0, 0,
arc_right[2]))
182         # Point at the right up corner:
183         pos_2 = (waveguide_length/2, waveguide_width/2)
184         points_waveguide.append((pos_2[0], pos_2[1], 0, 0, 0))
185         # Point at the left up corner
186         pos_3 = (-waveguide_length/2, waveguide_width/2)
187         arc_left = ezdf.math.arc_to_bulge((0,0), start_angle_rad
[1], final_angle_rad[1], R)
188         points_waveguide.append((pos_3[0], pos_3[1], 0, 0,
arc_left[2]))
189         # Point at the left down corner:
190         pos_4 = pos_0
191         points_waveguide.append((pos_4[0], pos_4[1], 0, 0, 0))
192     else:
193         R = d_waveguide_coupler + coupler_shift
194         # Point at the left down corner:
195         pos_0 = (-waveguide_length/2, -waveguide_width/2)
196         points_waveguide.append((pos_0[0], pos_0[1], 0, 0, 0))
197         # Point at the right down corner:
198         pos_1 = (waveguide_length/2, -waveguide_width/2)
199         points_waveguide.append((pos_1[0], pos_1[1], 0, 0, 0))
200         # Point at the right down extra corner:
201         pos_2 = sum_of_cart_coord(coupler_center_absolute[0],
pol2cart(R, start_angle_rad[0]))
202         arc_right = ezdf.math.arc_to_bulge((0,0),
start_angle_rad[0], final_angle_rad[0], R)
203         points_waveguide.append((pos_2[0], pos_2[1], 0, 0,
arc_right[2]))
204         # Point at the right up extra corner:
205         pos_3 = sum_of_cart_coord(coupler_center_absolute[0],
pol2cart(R, final_angle_rad[0]))
206         points_waveguide.append((pos_3[0], pos_3[1], 0, 0, 0))
207         # Point at the right up corner:
208         pos_4 = (waveguide_length/2, waveguide_width/2)
209         points_waveguide.append((pos_4[0], pos_4[1], 0, 0, 0))
210         # Point at the left up corner
211         pos_5 = (-waveguide_length/2, waveguide_width/2)
212         points_waveguide.append((pos_5[0], pos_5[1], 0, 0, 0))
213         # Point at the left up extra corner:
214         pos_6 = sum_of_cart_coord(coupler_center_absolute[1],
pol2cart(R, start_angle_rad[1]))
215         arc_left = ezdf.math.arc_to_bulge((0,0), start_angle_rad
[1], final_angle_rad[1], R)
216         points_waveguide.append((pos_6[0], pos_6[1], 0, 0,
arc_left[2]))
217         # Point at the left down extra corner:
218         pos_7 = sum_of_cart_coord(coupler_center_absolute[1],
pol2cart(R, final_angle_rad[1]))

```

```

219         points_waveguide.append((pos_7[0], pos_7[1], 0, 0, 0))
220         # Point at the left down corner:
221         pos_8 = pos_0
222         points_waveguide.append((pos_8[0], pos_8[1], 0, 0, 0))
223
224     msp.add_lwpolyline(points_waveguide)
225
226
227
228     # Design of the bragg couplers:
229     inner_radius = R-linewidth/2+distance_between_circles
230     radius_vector = [(inner_radius+distance_between_circles*i) for i
231                     in range(number_of_circles)]
232     for coupler in range(2):
233         for radius in radius_vector:
234             points_drawing = []
235             radius_pos = radius+linewidth/2
236             radius_neg = radius-linewidth/2
237
238             # Point for start_angle in small circle
239             pos_0 = sum_of_cart_coord(coupler_center_absolute[coupler
240 ], pol2cart(radius_neg, start_angle_rad[coupler]))
241             point_arc_0 = ezdf.math.arc_to_bulge((0,0),
242 start_angle_rad[coupler], final_angle_rad[coupler], radius_neg)
243             points_drawing.append((pos_0[0], pos_0[1], 0, 0,
244 point_arc_0[2]))
245             # Point for final_angle in small circle
246             pos_1 = sum_of_cart_coord(coupler_center_absolute[coupler
247 ], pol2cart(radius_neg, final_angle_rad[coupler]))
248             points_drawing.append((pos_1[0], pos_1[1], 0, 0, 0))
249             # Point for final_angle in big circle
250             pos_2 = sum_of_cart_coord(coupler_center_absolute[coupler
251 ], pol2cart(radius_pos, final_angle_rad[coupler]))
252             point_arc_2 = ezdf.math.arc_to_bulge((0,0),
253 start_angle_rad[coupler], final_angle_rad[coupler], radius_pos)
254             points_drawing.append((pos_2[0], pos_2[1], 0, 0, -
255 point_arc_2[2]))
256             # Point for start_angle in big circle
257             pos_3 = sum_of_cart_coord(coupler_center_absolute[coupler
258 ], pol2cart(radius_pos, start_angle_rad[coupler]))
259             points_drawing.append((pos_3[0], pos_3[1], 0, 0, 0))
260             # Point for start_angle in small circle
261             pos_4 = pos_0
262             points_drawing.append((pos_4[0], pos_4[1], 0, 0, 0))
263
264         msp.add_lwpolyline(points_drawing)
265
266
267
268     # Design of the contour:

```

```

259 separation_contour_inner = separation_contour
260 separation_contour_outer = separation_contour + width_contour
261 if add_contour == 1:
262     half_angle_coupler = (180-aperture_angle/2)/2
263     half_angle_coupler_rad = half_angle_coupler/180*math.pi
264     points_contour = []
265
266
267     # Inner contour variables:
268     x_shift_contour_inner = separation_contour_inner/np.tan(
269     half_angle_coupler_rad)
270
271     contour_inner_first_radius = (waveguide_width +
272     separation_contour_inner*2)/(2*np.sin(aperture_angle_rad/2))
273     contour_inner_shift = math.sqrt(contour_inner_first_radius
274     **2-(waveguide_width + separation_contour_inner*2)**2/4)
275     contour_inner_center_relative = (((waveguide_lenght-
276     x_shift_contour_inner*2)/2-contour_inner_shift, 0), (-((
277     waveguide_lenght-x_shift_contour_inner*2)/2-contour_inner_shift),
278     0))
279     contour_inner_center_absolute = (
280     contour_inner_center_relative[0], contour_inner_center_relative
281     [1])
282
283     final_inner_radius = ((radius_vector[-1] + linewidth/2) -
284     x_shift_contour_inner - coupler_first_radius) +
285     contour_inner_first_radius + separation_contour_inner
286     final_inner_radius_correction = (radius_vector[-1] +
287     linewidth/2) + separation_contour_inner
288     inner_aperture_angle_rad = (aperture_angle_rad*
289     final_inner_radius_correction + separation_contour_inner*2)/
290     final_inner_radius_correction
291     inner_aperture_angle = inner_aperture_angle_rad/math.pi*180
292     start_inner_angle_rad = -(inner_aperture_angle/2)/180*math.
293     pi, -(inner_aperture_angle/2)+180)/180*math.pi)
294     final_inner_angle_rad = ((inner_aperture_angle/2)/180*math.pi
295     , ((inner_aperture_angle/2)+180)/180*math.pi)
296
297     # Drawing of inner contour:
298     # Point at the left down corner:
299     pos_0 = (-waveguide_lenght/2 + x_shift_contour_inner, -
300     waveguide_width/2 - separation_contour_inner)
301     points_contour.append((pos_0[0], pos_0[1], 0, 0, 0))
302     # Point at the right down corner:
303     pos_1 = (waveguide_lenght/2 - x_shift_contour_inner, -
304     waveguide_width/2 - separation_contour_inner)
305     points_contour.append((pos_1[0], pos_1[1], 0, 0, 0))
306     # Point at the right down extra corner:

```

```

290     pos_2 = sum_of_cart_coord(contour_inner_center_absolute[0],
291     pol2cart(final_inner_radius, start_angle_rad[0]))
292     arc_right = ezdfx.math.arc_to_bulge((0,0),
293     start_inner_angle_rad[0], final_inner_angle_rad[0],
294     final_inner_radius_correction)
295     points_contour.append((pos_2[0], pos_2[1], 0, 0, arc_right
296     [2]))
297     # Point at the right up extra corner:
298     pos_3 = sum_of_cart_coord(contour_inner_center_absolute[0],
299     pol2cart(final_inner_radius, final_angle_rad[0]))
300     points_contour.append((pos_3[0], pos_3[1], 0, 0, 0))
301     # Point at the right up corner:
302     pos_4 = (waveguide_lenght/2 - x_shift_contour_inner,
303     waveguide_width/2 + separation_contour_inner)
304     points_contour.append((pos_4[0], pos_4[1], 0, 0, 0))
305     # Point at the left up corner
306     pos_5 = (-waveguide_lenght/2 + x_shift_contour_inner,
307     waveguide_width/2 + separation_contour_inner)
308     points_contour.append((pos_5[0], pos_5[1], 0, 0, 0))
309     # Point at the left up extra corner:
310     pos_6 = sum_of_cart_coord(contour_inner_center_absolute[1],
311     pol2cart(final_inner_radius, start_angle_rad[1]))
312     arc_left = ezdfx.math.arc_to_bulge((0,0),
313     start_inner_angle_rad[1], final_inner_angle_rad[1],
314     final_inner_radius_correction)
315     points_contour.append((pos_6[0], pos_6[1], 0, 0, arc_left[2])
316     )
317     # Point at the left down extra corner:
318     pos_7 = sum_of_cart_coord(contour_inner_center_absolute[1],
319     pol2cart(final_inner_radius, final_angle_rad[1]))
320     points_contour.append((pos_7[0], pos_7[1], 0, 0, 0))
321     # Point at the left down corner:
322     pos_8 = pos_0
323     points_contour.append((pos_8[0], pos_8[1], 0, 0, 0))
324
325     # Outer contour variables:
326     x_shift_contour_outer = separation_contour_outer/np.tan(
327     half_angle_coupler_rad)
328
329     contour_outer_first_radius = (waveguide_width +
330     separation_contour_outer*2)/(2*np.sin(aperture_angle_rad/2))
331     contour_outer_shift = math.sqrt(contour_outer_first_radius
332     **2-(waveguide_width + separation_contour_outer*2)**2/4)
333     contour_outer_center_relative = (((waveguide_lenght-
334     x_shift_contour_outer*2)/2-contour_outer_shift, 0), (-((
335     waveguide_lenght-x_shift_contour_outer*2)/2-contour_outer_shift)
336     , 0))

```

```

320     contour_outter_center_absolute = (
contour_outter_center_relative[0], contour_outter_center_relative
[1])
321
322     final_outter_radius = ((radius_vector[-1] + linewidth/2) -
x_shift_contour_outter - coupler_first_radius) +
contour_outter_first_radius + separation_contour_outter
323     final_outter_radius_correction = (radius_vector[-1] +
linewidth/2) + separation_contour_outter
324     outter_aperture_angle_rad = (aperture_angle_rad*
final_outter_radius_correction + separation_contour_outter*2)/
final_outter_radius_correction
325     outter_aperture_angle = outter_aperture_angle_rad/math.pi*180
326     start_outter_angle_rad = (-(outter_aperture_angle/2)/180*math
.pi, (-(outter_aperture_angle/2)+180)/180*math.pi)
327     final_outter_angle_rad = ((outter_aperture_angle/2)/180*math
.pi, ((outter_aperture_angle/2)+180)/180*math.pi)
328
329     # Drawing of outter contour:
330     # Point at the left down corner:
331     pos_9 = (-waveguide_lenght/2 + x_shift_contour_outter, -
waveguide_width/2 - separation_contour_outter)
332     points_contour.append((pos_9[0], pos_9[1], 0, 0, 0))
333     # Point at the left down extra corner:
334     pos_10 = sum_of_cart_coord(contour_outter_center_absolute[1],
pol2cart(final_outter_radius, final_angle_rad[1]))
335     arc_left = ezdxf.math.arc_to_bulge((0,0),
start_outter_angle_rad[1], final_outter_angle_rad[1],
final_outter_radius_correction)
336     points_contour.append((pos_10[0], pos_10[1], 0, 0, -arc_left
[2]))
337     # Point at the left up extra corner:
338     pos_11 = sum_of_cart_coord(contour_outter_center_absolute[1],
pol2cart(final_outter_radius, start_angle_rad[1]))
339     points_contour.append((pos_11[0], pos_11[1], 0, 0, 0))
340     # Point at the left up corner
341     pos_12 = (-waveguide_lenght/2 + x_shift_contour_outter,
waveguide_width/2 + separation_contour_outter)
342     points_contour.append((pos_12[0], pos_12[1], 0, 0, 0))
343     # Point at the right up corner:
344     pos_13 = (waveguide_lenght/2 - x_shift_contour_outter,
waveguide_width/2 + separation_contour_outter)
345     points_contour.append((pos_13[0], pos_13[1], 0, 0, 0))
346     # Point at the right up extra corner:
347     pos_14 = sum_of_cart_coord(contour_outter_center_absolute[0],
pol2cart(final_outter_radius, final_angle_rad[0]))
348     arc_right = ezdxf.math.arc_to_bulge((0,0),
start_outter_angle_rad[0], final_outter_angle_rad[0],
final_outter_radius_correction)

```

```

349     points_contour.append((pos_14[0], pos_14[1], 0, 0, -arc_right
350 [2]))
351     # Point at the right down extra corner:
352     pos_15 = sum_of_cart_coord(contour_outter_center_absolute[0],
353     pol2cart(final_outter_radius, start_angle_rad[0]))
354     points_contour.append((pos_15[0], pos_15[1], 0, 0, 0))
355     # Point at the right down corner:
356     pos_16 = (waveguide_lenght/2 - x_shift_contour_outter, -
357     waveguide_width/2 - separation_contour_outter)
358     points_contour.append((pos_16[0], pos_16[1], 0, 0, 0))
359     # Point at the left down corner:
360     pos_17 = pos_9
361     points_contour.append((pos_17[0], pos_17[1], 0, 0, 0))
362     # Point at the left down corner:
363     pos_18 = pos_0
364     points_contour.append((pos_18[0], pos_18[1], 0, 0, 0))
365
366     msp.add_lwpolyline(points_contour)
367
368     # save the DXF document
369     doc.saveas("line.dxf")
370
371     # Calculate the center in x of both gratings:
372     angles_0_pi = [0, math.pi]
373     for coupler in range(2):
374         radius_for_center_min = radius_vector[0] - linewidth/2
375         position_a = sum_of_cart_coord(coupler_center_absolute[
376     coupler], pol2cart(radius_for_center_min, start_angle_rad[coupler
377     ]))
378         position_a_x = position_a[0]
379
380         radius_for_center_max = radius_vector[-1] + linewidth/2
381         position_b = sum_of_cart_coord(coupler_center_absolute[
382     coupler], pol2cart(radius_for_center_max, angles_0_pi[coupler]))
383         position_b_x = position_b[0]
384
385         center_grating = (position_a_x + position_b_x)/2
386
387         file_txt.write(str(center_grating))
388         file_txt.write('\n') # End of the line
389
390     print("Done")
391
392     window = tk.Tk() # Instantiate and instance of a window
393     window.geometry("350x1000")
394     window.title("Optical Resonator Designer")
395     window.config()

```

```
392 |
393 | # Initialize the fields:
394 | fields = {}
395 |
396 | # Waveguide width:
397 | fields['waveguide_width_label'] = tk.Label(text='Waveguide width (um)
398 | :')
399 | fields['waveguide_width'] = tk.Entry()
400 | fields['waveguide_width'].insert(0, str(2))
401 |
402 | # Waveguide lenght:
403 | fields['waveguide_lenght_label'] = tk.Label(text='Waveguide lenght (
404 | um):')
405 | fields['waveguide_lenght'] = tk.Entry()
406 | fields['waveguide_lenght'].insert(0, str(200))
407 |
408 | # Linewidth:
409 | fields['linewidth_label'] = tk.Label(text='Linewidth (um):')
410 | fields['linewidth'] = tk.Entry()
411 | fields['linewidth'].insert(0, str(0.314))
412 |
413 | # Distance between circles:
414 | fields['distance_between_circles_label'] = tk.Label(text='Coupler
415 | period (um):')
416 | fields['distance_between_circles'] = tk.Entry()
417 | fields['distance_between_circles'].insert(0, str(0.628))
418 |
419 | # Number of circles:
420 | fields['number_of_circles_label'] = tk.Label(text='Number of circle
421 | segments:')
422 | fields['number_of_circles'] = tk.Entry()
423 | fields['number_of_circles'].insert(0, str(163))
424 |
425 | # Aperture angle:
426 | fields['aperture_angle_label'] = tk.Label(text='Aperture angle (
427 | degrees):')
428 | fields['aperture_angle'] = tk.Entry()
429 | fields['aperture_angle'].insert(0, str(40))
430 |
431 | # Distance from waveguide edge to bragg coupler:
432 | fields['d_waveguide_coupler_label'] = tk.Label(text='Distance from
433 | waveguide edge to bragg coupler (um):')
434 | fields['d_waveguide_coupler'] = tk.Entry()
435 | fields['d_waveguide_coupler'].insert(0, str(5))
436 |
437 | # Add contour to the design:
438 | fields['add_contour_label'] = tk.Label(text='Add contour to the
439 | design (1 for yes, 0 for no):')
440 | fields['add_contour'] = tk.Entry()
```

```
434 fields['add_contour'].insert(0, str(0))
435
436 # Distance of separation of the contour:
437 fields['separation_contour_label'] = tk.Label(text='Distance of
    separation of the contour (um):')
438 fields['separation_contour'] = tk.Entry()
439 fields['separation_contour'].insert(0, str(0.308))
440
441 # Width of the contour:
442 fields['width_contour_label'] = tk.Label(text='Width of the contour (
    um):')
443 fields['width_contour'] = tk.Entry()
444 fields['width_contour'].insert(0, str(0.200))
445
446 # Add Distributed Bragg Reflector to the design:
447 fields['add_dbr_label'] = tk.Label(text='Add DBR to the design (1 for
    yes, 0 for no):')
448 fields['add_dbr'] = tk.Entry()
449 fields['add_dbr'].insert(0, str(0))
450
451 # Cavity lenght:
452 fields['dbr_cavity_lenght_label'] = tk.Label(text='DBR Cavity lenght
    (um):')
453 fields['dbr_cavity_lenght'] = tk.Entry()
454 fields['dbr_cavity_lenght'].insert(0, str(0.245))
455
456 # Bragg period:
457 fields['dbr_period_label'] = tk.Label(text='DBR period (um):')
458 fields['dbr_period'] = tk.Entry()
459 fields['dbr_period'].insert(0, str(0.245))
460
461 # Bragg linewidth:
462 fields['dbr_linewidth_label'] = tk.Label(text='DBR linewidth (um):')
463 fields['dbr_linewidth'] = tk.Entry()
464 fields['dbr_linewidth'].insert(0, str(0.1225))
465
466 # Bragg # of lines:
467 fields['dbr_number_lines_label'] = tk.Label(text='DBR number of lines
    :')
468 fields['dbr_number_lines'] = tk.Entry()
469 fields['dbr_number_lines'].insert(0, str(2))
470
471
472
473
474 for field in fields.values():
475     field.pack(anchor=tk.W, padx=10, pady=5, fill=tk.X)
476
```

```
477 tk.Button(text='Draw waveguide with grating coupler', command=  
    draw_waveguide_coupler).pack(anchor=tk.W, padx=10, pady=5, fill=tk  
    .X)  
478  
479 file_txt = open('Eq_grating_distances.txt', 'w')  
480  
481  
482 window.mainloop()
```

Bibliography

- [1] *Integrated microwave to optical conversion on a superconducting atom chip*. QuantERA. URL: <https://quantera.eu/moca/> (cit. on p. 1).
- [2] D. Petrosyan, K. Mølmer, J. Fortágh, and M. Saffman. «Microwave to optical conversion with atoms on a superconducting chip». In: *New Journal of Physics* 21.7 (July 2019), p. 073033. DOI: 10.1088/1367-2630/ab307c. URL: <https://dx.doi.org/10.1088/1367-2630/ab307c> (cit. on p. 2).
- [3] Á. Kurkó et al. «Optimal collection of radiation emitted by a trapped atomic ensemble». In: *EPJ Quantum Technology* 8.1 (May 2021), p. 11. DOI: 10.1140/epjqt/s40507-021-00102-1. URL: <https://doi.org/10.1140/epjqt/s40507-021-00102-1> (cit. on p. 2).
- [4] Anonymous. «Proceedings of the American Physical Society». In: *Phys. Rev.* 69 (11-12 June 1946), pp. 674–674. DOI: 10.1103/PhysRev.69.674.2. URL: <https://link.aps.org/doi/10.1103/PhysRev.69.674.2> (cit. on p. 2).
- [5] Dr. R. Paschotta. *Waveguides*. URL: <https://www.rp-photonics.com/waveguides.html> (cit. on p. 6).
- [6] G. Ghione. *Notes from the course: Photonic Devices*. Torino, 2022 (cit. on p. 8).
- [7] L. Chrostowski and M. Hochberg. *Silicon Photonics Design: From devices to systems*. Cambridge University Press, 2015 (cit. on pp. 8, 9, 11, 13, 14, 18–20).
- [8] *COMSOL Multiphysics*. URL: <https://www.comsol.com/> (cit. on p. 9).
- [9] COMSOL. *RF Module*. URL: <https://www.comsol.com/rf-module> (cit. on p. 10).
- [10] A. Perot and C. Fabry. «On the Application of Interference Phenomena to the Solution of Various Problems of Spectroscopy and Metrology». In: 9 (Feb. 1899), p. 87. DOI: 10.1086/140557. URL: <https://ui.adsabs.harvard.edu/abs/1899ApJ....9...87P/abstract> (cit. on p. 12).

- [11] L. Cheng, S. Mao, Z. Li, Y. Han, and H. Y. Fu. «Grating Couplers on Silicon Photonics: Design Principles, Emerging Trends and Practical Issues». In: *Micromachines* 11.7 (2020). ISSN: 2072-666X. DOI: 10.3390/mi11070666. URL: <https://www.mdpi.com/2072-666X/11/7/666> (cit. on p. 15).
- [12] Dr. R. Paschotta. *Mode Radius*. URL: https://www.rp-photonics.com/mode_radius.html (cit. on p. 15).
- [13] ThorLabs. *Single Mode Fiber*. URL: https://www.thorlabs.com/newgroup_page9.cfm?objectgroup_id=949 (cit. on p. 15).
- [14] Dr. R. Paschotta. *Optical Resonators*. URL: [https://www.rp-photonics.com/optical_resonators.html#:~:text=An%20optical%20resonator%20\(or%20resonant,made%20in%20very%20different%20forms.](https://www.rp-photonics.com/optical_resonators.html#:~:text=An%20optical%20resonator%20(or%20resonant,made%20in%20very%20different%20forms.) (cit. on p. 17).
- [15] P. Bardella. *Notes from the course: Photonic Devices*. Torino, 2022 (cit. on pp. 18, 19).
- [16] M. Cocuzza. *Notes from the course: Physics of technological processes*. Torino, 2021 (cit. on pp. 22, 35, 38, 40, 43, 51).
- [17] Oxford Instruments. *PlasmaPro 100 ICPCVD*. URL: <https://plasma.oxinst.com/products/icpcvd/plasmapro-100-icpcvd> (cit. on p. 24).
- [18] S. Thomas. «Chapter 10 - Mass spectrometry». In: *Contemporary Practice in Clinical Chemistry (Fourth Edition)*. Ed. by Willia Clarke and Mark A. Marzinke. Fourth Edition. Academic Press, 2019, pp. 171–185. ISBN: 978-0-12-815499-1. DOI: <https://doi.org/10.1016/B978-0-12-815499-1.00010-7>. URL: <https://www.sciencedirect.com/science/article/pii/B9780128154991000107> (cit. on p. 24).
- [19] J. W. Lee, K. D. Mackenzie, D. Johnson, J. N. Sasserath, S. J. Pearton, and F. Ren. «Low Temperature Silicon Nitride and Silicon Dioxide Film Processing by Inductively Coupled Plasma Chemical Vapor Deposition». In: *Journal of The Electrochemical Society* 147.4 (Apr. 2000), p. 1481. DOI: 10.1149/1.1393382. URL: <https://dx.doi.org/10.1149/1.1393382> (cit. on p. 24).
- [20] J.A. Woollam. *What is ellipsometry?* URL: <https://www.jawoollam.com/resources/ellipsometry-tutorial/what-is-ellipsometry> (cit. on p. 25).
- [21] J.A. Woollam. *CompleteEASE Software Manual*. URL: https://wiki.nanofab.ucsb.edu/w/images/2/2e/CompleteEASE_Manual.pdf (cit. on p. 26).
- [22] M. Rajankunte. *Optical Profilometer*. 2022. URL: <https://www.tribonet.org/wiki/optical-profilometer/> (cit. on p. 27).

- [23] A. Bakhtazad and S. Chowdhury. «An evaluation of optical profilometry techniques for CMUT characterization». In: *Microsystem Technologies* 25.9 (Sept. 2019), pp. 3627–3642. DOI: 10.1007/s00542-019-04377-4. URL: <https://doi.org/10.1007/s00542-019-04377-4> (cit. on p. 28).
- [24] NanoScience Instruments. *Profilometry*. URL: <https://www.nanoscience.com/techniques/profilometry/> (cit. on p. 30).
- [25] D. Mogk. *X-Ray Photoelectron Spectroscopy (XPS; aka Electron Spectroscopy for Chemical Analysis, ESCA)*. Imaging and Chemical Analysis Laboratory, Montana State University. URL: https://serc.carleton.edu/msu_nanotech/methods/xps.html (cit. on p. 33).
- [26] Columbia University. *HEIDELBERG μ PG 101 LASER WRITER*. 2016. URL: <https://cni.columbia.edu/heidelberg-pg-101-laser-writer> (cit. on p. 35).
- [27] S. Swapp. *Scanning Electron Microscopy (SEM)*. University of Wyoming. URL: https://serc.carleton.edu/research_education/geochemsheets/techniques/SEM.html (cit. on p. 41).
- [28] Kayaku Advanced Materials. *OmniCoat*. URL: <https://kayakuam.com/wp-content/uploads/2021/07/KAM-OmniCoat-Datasheet-11.19.20-final.pdf> (cit. on p. 43).
- [29] JC Nability Lithography Systems. *Nanometer Pattern Generation System*. URL: <https://www.jcnability.com/> (cit. on p. 44).
- [30] Dr A. Goodyear. *Automatic Endpoint Detection*. Oxford. URL: <https://plasma.oxinst.com/blog/2020/automatic-endpoint-detection> (cit. on p. 52).
- [31] *The basics of the Bosch Process (Silicon Deep RIE)*. SAMCO. URL: <https://www.samcointl.com/basics-bosch-process-silicon-deep-rie/> (cit. on p. 53).
- [32] M. D. Henry, S. Walavalkar, A. Homyk, and A. Scherer. «Alumina etch masks for fabrication of high-aspect-ratio silicon micropillars and nanopillars». In: *Nanotechnology* 20.25 (June 2009), p. 255305. DOI: 10.1088/0957-4484/20/25/255305. URL: <https://dx.doi.org/10.1088/0957-4484/20/25/255305> (cit. on p. 55).
- [33] *Automatic Endpoint Detectors*. Oxford. URL: <https://plasma.oxinst.com/service-support/upgrades/optical-end-point-detectors> (cit. on p. 57).
- [34] E. Hecht. *Optics*. Pearson education. Addison-Wesley, 2002. ISBN: 9780321188786| URL: <https://books.google.it/books?id=T3ofAQAAMAAJ> (cit. on p. 61).

- [35] V. Bonino and A. Angelini. «High-Q Fano resonances in diamond nanopillars». In: *Opt. Mater. Express* 13.4 (Apr. 2023), pp. 1110–1117. DOI: 10.1364/OME.484614. URL: <https://opg.optica.org/ome/abstract.cfm?URI=ome-13-4-1110> (cit. on p. 65).
- [36] A. T. Young. «Rayleigh scattering». In: 20.4 (Feb. 1981), pp. 533–535. DOI: 10.1364/AO.20.000533. URL: <https://ui.adsabs.harvard.edu/abs/1981ApOpt..20..533Y> (cit. on p. 67).
- [37] D. Leith. «Light Scattering Theory». In: 2018. URL: <https://api.semanticscholar.org/CorpusID:125880371> (cit. on p. 67).
- [38] M. Kerker, D.-S. Wang, and C. L. Giles. «Electromagnetic scattering by magnetic spheres». In: *J. Opt. Soc. Am.* 73.6 (June 1983), pp. 765–767. DOI: 10.1364/JOSA.73.000765. URL: <https://opg.optica.org/abstract.cfm?URI=josa-73-6-765> (cit. on p. 68).